



Archaean Zircon U-Pb Age Paradox in Juvenile Neoproterozoic Granitoids, Central North Sudan, Saharan Metacraton

SHANG COSMAS KONGNYUY¹, MORTEANI GIULIO² & MUHARREM SATIR¹

¹ University of Tübingen, Institute of Geosciences, Wilhelmstrasse 56, 72074 Tübingen, Germany
(E-mail: cosmas@uni-tuebingen.de ; shang004@yahoo.com)

² Technical University of Munich, Gmain Nr.1, 84424 Isen, Germany

Received 09 February 2010; revised typescripts received 30 October 2010 & 07 December 2010; accepted 23 January 2011

Abstract: It has long been shown that central North Sudan with its heterogeneous isotopic composition, unlike neighbouring Archaean cratons and the Neoproterozoic Arabian-Nubian Shield, is part of the Saharan metacratonic crust that was remobilized in the Neoproterozoic. In this paper, we report an Archaean zircon U-Pb age in the Saharan Metacraton that paradoxically does not indicate the presence of an Archaean crust. The second paradox concerns geochemical data that show Archaean tonalite-trondjemite-granodiorite (TTG) features and also post-Archaean granitoid features, yet the rocks are Neoproterozoic. The granitoids studied are from north of Delgo in the Halfa terrane. They are calc-alkaline and meta- to peraluminous and have negative Nb and Ti anomalies. Zircon morphology, cathodoluminescence (CL) and U-Pb age data define four magmatic zircon populations. The oldest is characterized by a 3025 Ma Archaean U-Pb age. The 728 to 702 Ma ages of the second zircon population suggest that the studied area was involved in the Neoproterozoic intraplate magmatism that was induced by the delamination of the thickened asthenospheric mantle due to the first collisional contact between East and West Gondwana. Zircons of the third group yield peak Pan-African orogeny Neoproterozoic ages (630 to 600 Ma) that are identical with titanite age data, and show that the studied rocks were intensely remobilized by the Pan-African tectono-metamorphic regional event. Lastly, the 554 Ma concordant zircon of the fourth population suggests that the area thereafter never again experienced such high temperature and pressure regional orogenic effects. Sr initial values (0.702389–0.704011) and ϵ_{Nd} values (+5.05±8.66) indicate juvenile sources with insignificant crustal contribution. Nd TDM ages are Neoproterozoic (917–653 Ma) and identical within error and/or slightly older than the Neoproterozoic zircon ages, confirming the primitive nature of this magmatism. This sets a paradox with the Archaean zircon population in these rocks, implying that this zircon population is xenocrystic and has no bearing to the age of the tract of terrane investigated. These results show that combining zircon U-Pb ages and Nd isotope systematics is a very powerful tool in unequivocally defining the petrogenesis of rocks and geological terranes.

Key Words: zircon populations, Archaean zircon U-Pb age paradox, Nd TDM, petrogenesis, juvenile sources, Neoproterozoic

Juvenil Neoproterozoyik Granitoyidlerindeki Arkeyan Zirkon U-Pb Yaş Çelişkisi, Orta Kuzey Sudan, Saharan Metakratonu

Özet: Orta Kuzey Sudan'ın, komşu Arkeyan kratonlarının ve Neoproterozoyik Arabian-Nubian Kalkanı'nın aksine, heterojen izotopik bileşime sahip olduğu ve Neoproterozoyik'te tekrar hareketlenmiş olan Saharan Metakratonik kabuğunun bir parçası olduğu uzun zamandır gösterilmekteydi. Biz bu makalede Saharan Metakratonu'nda, çelişkili olarak, Arkeyan kabuğun varlığına işaret etmeyen Arkeyan zirkon U-Pb yaşları sunacağız. İkinci çelişki ise kayaçlar Neoproterozoyik olduğu halde, hem Arkeyan tonalit-tronjemit-granodiyorit (TTG) özellikleri hem de Arkeyan-sonrası granitoyid özellikleri sergileyen jeokimyasal verileri kapsamaktadır. Çalışılan granitoyidler Halfa Terreni'nde Delgo'nun kuzeyindedir. Kayaçlar, kalk-alkalen ve metaalüminaldan peralüminalıya geçişli olup, negatif Nb ve Ti sapmalarına sahiptir. Zirkon morfolojisi, katodoluminesans (CL) ve U-Pb yaş verileri dört magmatik zirkon popülasyonunu tanımlamaktadır. En yaşlısı, 3025 My Arkeyan U-Pb yaşıyla karakterize edilmektedir. İkinci zirkon popülasyonunun 728–702 My arası yaşları, araştırma alanının, Doğu ve Batı Gondwana'nın ilk çarpışma kontağı nedeniyle kalınlaşmış astenosferik mantonun delaminasyonunun yol açtığı Neoproterozoyik levha-içi magmatizmanın içerisinde yeraldığını önermektedir. Üçüncü grubun zirkonları, titanit yaşlarıyla özdeş olan ve çalışılan kayaçların bölgesel Pan-Afrikan tektono-metamorfik olaylarıyla birlikte yoğun olarak tekrardan hareketlendiğini gösteren, doruk Pan-Afrikan

orojenezi Neoproterozoyik yaşları (630–600 My) vermektedir. Son olarak, dördüncü popülasyonun 554 My yaşlı konkordan zirkonları, alanın daha sonra asla böylesine yüksek sıcaklık ve bölgesel orojenik etkiler geçirmediği önerisini getirmektedir. İlksel Sr (0.702389–0.704011) ve ϵ_{Nd} (+5.05±8.66) değerleri önemsiz kıtasal kabuk kirlenmesine uğramış juvenil kaynaklara işaret etmektedir. Nd TDM yaşlarının, Neoproterozoyik (917–653 Ma) olması ve Neoproterozoyik zirkon yaşlarıyla hata payı içinde özdeş olması ve/veya bunlardan kısmen yaşlı olması, bu magmatizmanın primitif özelliğini teyid etmektedir. Bu da, bu zirkon popülasyonunun zenokristik olduğunu ve incelenen terreyinin alanına ait yaşları içermediğini ortaya koyarak, bu kayalardaki Arkeyan zirkon popülasyonu çelişkinsini çözmektedir. Bu sonuçlar, zirkon U-Pb yaşları ile Nd izotop sistematığının birleştirilmesinin, kayaların petrolojisinin ve jeolojik terreyinlerin açık bir şekilde tanımlanmasında çok güçlü bir araç olduğunu göstermektedir.

Anahtar Sözcükler: zirkon popülasyonları, Arkeyan zirkon U-Pb yaş çelişkisi, Nd TDM, petrojenez, juvenile kaynaklar, Neoproterozoyik

Introduction

Available geochronological data from the Saharan Metacraton (Abdelsalam *et al.* 2002 and references therein; Küster *et al.* 2008) suggest that the oldest rocks exposed are Archaean-Palaeoproterozoic formations, including migmatites, charnockites and granulites, occurring at Uweynat, a belt at the boundary between Libya, Egypt and Sudan (Figure 1). Relatively old ages (1950–2700 Ma; Eburnean to Archaean) have also long been reported from many parts of the Saharan Metacraton including the Central African Republic, Western Sudan, Chad and Egypt (e.g., Hashad *et al.* 1972; El Shazly *et al.* 1973; Klerkx & Deutsch 1977; Cahen *et al.* 1984), and recently from the El Melagi gneisses of the Bayuda desert, Sudan (e.g., 2500–2700 Ma; Küster *et al.* 2008). Otherwise, old ages are given by detrital zircons from granulites, e.g., Archaean (2650 Ma) detrital zircons in the Sabaloka granulites (e.g., Kröner *et al.* 1987). The rest of the Saharan Metacraton comprises mostly granitoids and granulites, paragneisses and various schists with imprints of several fold stages (e.g., Fleck *et al.* 1973; Huth *et al.* 1984), giving Neoproterozoic radiometric ages between 500 and 700 Ma that correspond to the Pan-African tectonothermal event (e.g., Kennedy 1965), including the time of the East and West Gondwana collision (e.g., Shang *et al.* 2010a). Using the zircon radiometric data, the overall geochronological frame of the Saharan Metacraton formations shows few Archaean and abundant Mesoproterozoic and Neoproterozoic zircon crystallisation ages, confirmed by similar Nd TDM ages, the two being characteristics that define real tracts of terrane. Pb, Sr and Nd isotope compositions frequently display crustal signatures, juvenile ones as well as mixtures between the two.

Combined geochronological and isotopic data thus define the Saharan Metacraton as a heterogeneous terrane (Abdelsalam *et al.* 2002 and references therein; Küster *et al.* 2008) strongly overprinted by the Neoproterozoic Pan-African tectonothermal event (Shang *et al.* 2010a). Many more features of this heterogeneous nature of the Saharan Metacraton may still be revealed. In this paper we present new geochemical, geochronological and isotopic data from a granitic basement that crops out near Abu Sari, north of Delgo in central North Sudan (Figure 2). We will show the presence of a TTG-like rock association with Archaean features including zircon ages and demonstrate a paradox using Nd TDM ages that Archaean zircon ages do not necessarily define an old tract of terrane. Instead, a primitive Neoproterozoic basement would be defined.

Geological Setting

The studied area is situated in central North Sudan near Abu Sari, north of the city of Delgo (Figure 2). It is part of the Neoproterozoic to Archaean heterogeneous Saharan Metacraton (Abdelsalam *et al.* 2002 and references therein; Küster *et al.* 2008; Liégeois & Stern 2009; Shang *et al.* 2010a) that includes the area between the Archaean Congo Craton in the south, the Tuareg Shield in the west, and the mostly Neoproterozoic Arabian-Nubian Shield in the east (Figure 1a). The Saharan Metacraton consists of uplifted Precambrian massifs overlain by Cretaceous and younger cover rocks. It is thought to be a decratonized terrane (Black & Liégeois 1993; Liégeois *et al.* 1994), derived from coherent pre-Neoproterozoic continental crust (Dostal *et al.* 1985; Schandelmeyer *et al.* 1990, 1994;

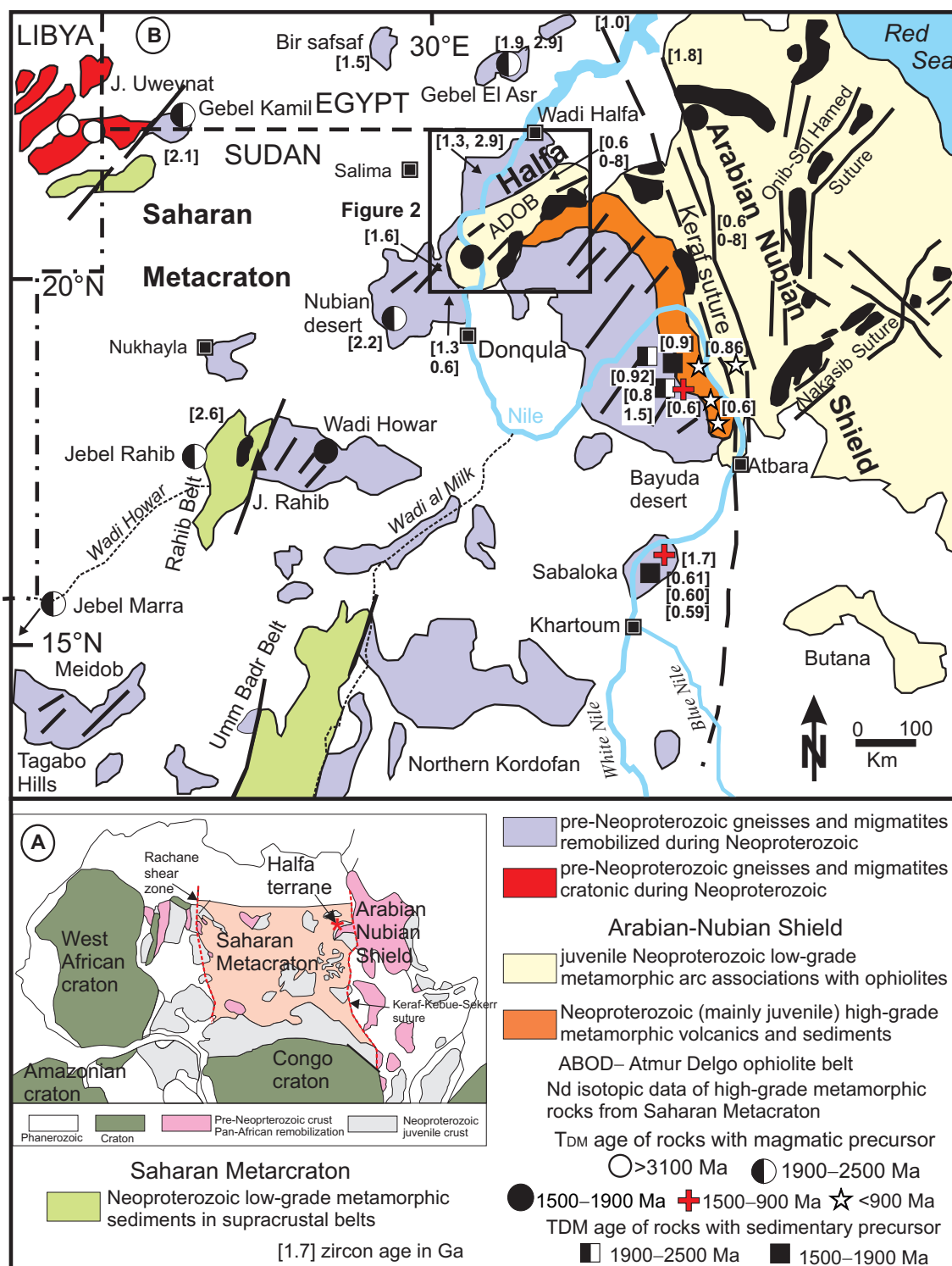


Figure 1. (a) Location of the Saharan Metacraton, the study area and neighbouring terranes in the geological map of Africa north of the Equator in the Neoproterozoic, also showing parts of the Amazonia Craton in Brazil; (b) geological sketch map of northeastern part of the Saharan Metacraton with major lithostructural units, modified after Küster *et al.* (2008). Nd isotopic data and U-Pb ages are from Stern *et al.* (1994), Küster *et al.* (2008) and references therein and Shang *et al.* (2010a, b).

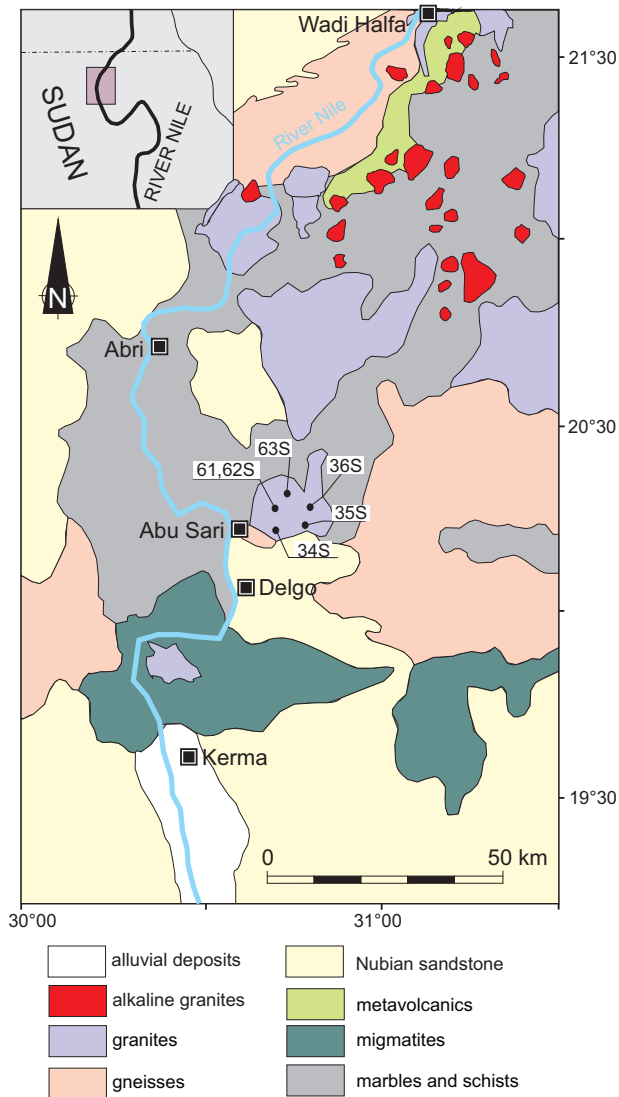


Figure 2. Simplified geological map of the Halfa terrane, central North Sudan, showing the crystalline basement and supracrustal formations, location of the studied basement outcrop and the analyzed samples.

Stern *et al.* 1994), or a collage of exotic terranes assembled in the Neoproterozoic (Küster & Liégeois 2001). The concept of the Saharan Metacraton (e.g., Abdelsalam *et al.* 2002) thus implies that during the Neoproterozoic Pan-African orogenic cycle (900–550 Ma) the Saharan basement neither behaved as a stable craton nor as a classical mobile belt. Instead, Late Neoproterozoic events remobilized the Archaean to Early Neoproterozoic continental crust by intense metamorphism, granitoid magmatism and deformation, leading to a variety of isotopic and

radiometric ages, hence the heterogeneous signature of this terrane.

Rocks of the Saharan Metacraton are patchily exposed in northwestern Sudan, central North Sudan and in southwestern Egypt (Figure 1b). Nd isotopic data from the high-grade basement suggest crustal growth direction from the northeastern Saharan Metacraton to the southeast (Küster *et al.* 2008). In the northeast, the Archaean crust of the Uweynat massif (Nd TDM ages > 3100 Ma; Harris *et al.* 1984; Figure 1) was not remobilized during the Neoproterozoic (e.g., Klerkx & Deutsch 1977), but was intruded by Cenozoic alkaline ring-complexes (André *et al.* 1991; Conticelli *et al.* 1995). The Uweynat massif is therefore just a preserved part of the metacraton but is no longer truly cratonic. In southwestern Egypt (Gebel Kamil and Gebel El Asr localities), northwestern Sudan (Nubian desert and Gebel Rahib) and western Sudan (Gebel Marra region), isotopic data from tonalitic and granitic orthogneisses and from migmatites have confirmed the existence of mainly Palaeoproterozoic crust (Nd TDM ages between 1900–2500 Ma; Harris *et al.* 1984; Harms *et al.* 1990). Slightly younger Nd TDM ages of 1600–1700 Ma have been reported in tonalitic gneisses at Wadi Howar (Harms *et al.* 1990). This Palaeoproterozoic basement was intensely remobilized and deformed during the Neoproterozoic Pan-African orogeny (Harms *et al.* 1990; Schandelmeier *et al.* 1990).

To the southeast in the Bayuda Desert and at Sabaloka (Figure 1b), medium- to high-grade metasedimentary schists and gneisses have Nd TDM ages between 1600 and 2200 Ma (Harris *et al.* 1984; Kröner *et al.* 1987; Küster & Liégeois 2001), while granitic orthogneisses from the Bayuda Desert have Palaeoproterozoic Nd TDM ages between 2000 and 2400 Ma (Küster & Liégeois 2001). Metagranitoids in the El Melagi terrane, however, record a 920–900 Ma Bayudian orogenic event (Küster *et al.* 2008). This terrane appears only slightly affected by younger Pan-African tectogenesis and deformation. It has a predominantly Late Archaean to Palaeoproterozoic source region and a Grenvillian deposition age for its pelitic precursor (Küster *et al.* 2008). Isotope characteristics of the Absol series, comprising various mica schists: quartz-mica schist, kyanite-staurolite-

garnet-mica schist, tourmaline mica schist, graphitic and manganiferous schist, ferruginous quartzite, amphibolites and hornblende gneisses, indicate progressive assimilation of old pre-Neoproterozoic crust.

Post-collisional late Pan-African (620–560 Ma) high-K granites are abundant in the entire northeastern Saharan Metacraton, except in the Uweinat massif. This granitoid magmatism is contemporaneous with escape tectonics along major strike-slip shear zones, uplift and extension of the entire Pan-African orogen in northeastern Africa (Stern 1994; Küster & Harms 1998).

The Halfa terrane in central North Sudan (Figure 1b) that contains our study area (Figure 2), consists of five principal lithologies: (1) strongly foliated high-grade gneissic rocks (the Duweishat gneisses e.g., Stern *et al.* 1994), the coeval North Kerma migmatitic gneisses and granites (Shang *et al.* 2010a), unconformably overlain by an amphibolite grade less-deformed supracrustal succession; (2) mafic metavolcanics; (3) metasediments and predominantly felsic metavolcanics, marbles and greenschists of the Atmur Delgo belt (Denkler *et al.* 1994; Schandelmeier *et al.* 1994; Stern *et al.* 1994); (4) syntectonic granodiorites; and (5) anorogenic alkaline granites (Shang *et al.* 2010b). Migmatitic gneisses yield 2.81–1.26 Ga Nd model ages ascribed to pre-Neoproterozoic precursors. They are marked by Type III Pb ratios and strongly negative $\epsilon_{\text{Nd}(t)}$ values but also yield younger Rb-Sr ages, indicating extensive Neoproterozoic overprinting (Harms *et al.* 1990, 1994; Stern *et al.* 1994; Shang *et al.* 2010a). Although now in fault contact, it is believed that the supracrustal rocks of the Halfa terrane were originally deposited during the opening and closing of an oceanic basin or re-entrant above a NW-dipping subduction zone at the eastern margin of the Saharan Metacraton (Schandelmeier *et al.* 1994).

Petrography

The studied samples were collected from an outcrop north of Delgo (Figure 2). They mainly occur as ground level exposures and as small mounds, revealing leucocratic, pink, grey, and dark grey,

mostly coarse-grained rocks with marked variation in their fabric, comprising a granitic and gneissic facies (Figure 3) with localized migmatitic textures. Three main facies were observed: (1) massive heterogranular texture (non-foliated), with zoned centimetre-size pinkish feldspar phenocrysts observable with the naked eye, in a dominantly mafic medium-grained matrix (Figure 3a; sample 36S); (2) slightly foliated mesocratic rocks with relatively few feldspar phenocrysts and mafics and more abundant medium-grained pale phases (Figure 3b; sample 62S) than in (1); (3) strongly foliated medium-grained grey facies with discontinuous streaks of dark grey mafic phases alternating with light grey quartzofeldspathic streaks characterized by glassy quartz and whitish feldspars (Figure 3c; sample 34S). Despite these textural dissimilarities, the bulk mineralogy is more or less the same. Essential components include plagioclase, K-feldspar, quartz, hornblende and biotite with titanite, zircon, apatite and opaques as accessory minerals. Widespread late-stage alteration is manifest in thin sections as chloritization, seritization and epidotization.

Plagioclase (An_{5-27}) occurs both as zoned phenocrysts (Figure 4a) and smaller crystals. Altered phases show strong seritization (Figure 4c, f). Microcline is the principal K-feldspar (Figure 4b, d). Microcline phenocrysts often have plagioclase and biotite inclusions (Figure 4b). Perthitic textures are common. Myrmekites often occur at contacts between K-feldspar and plagioclase, a usual mode of formation (Figure 4g). Larger-scale graphic texture is also abundantly displayed (Figure 4f). Graphic intergrowth is typical of intraplate granites. It marks the final crystallization stage and rarely survives later thermotectonic overprint. Quartz is generally abundant, occurring as microcrysts with contoured grain boundaries (Figure 4e).

Mafic phases are largely represented by idiomorphic green hornblende, commonly twinned, as well as reddish green biotite flakes in fresh rock sections (Figure 4a, b, h), while in altered sections, epidote largely replaces amphibole (Figure 5g) and plagioclase, and chlorite replaces biotite (Figure 4c, e). Titanite is characterized by large euhedral crystals (Figure 4d), while slender grains of zoned zircon occur as inclusions in biotite (Figure 4h).



Figure 3. Hand specimens showing some structural varieties of the samples studied: (a) centimetre size pink feldspar phenocrysts in a dominantly mafic-rich medium-grained matrix (sample 36S); (b) slightly foliated mesocratic sample, heterogranular with more abundant medium-grained light-coloured phases (sample 62S); (c) light grey and foliated sample, medium-grained with discontinuous streaks of dark grey mafic phases alternating with thicker light grey coloured quartzo-feldspathic bands characterized by glassy quartz and whitish feldspars (sample 34S).

Analytical Techniques

Whole-rock geochemical and isotopic analyses were performed at the University of Tübingen. Major and trace elements were measured on fused glass beads of whole-rock powders, using a Bruker AXS S4 Pioneer spectrometer and standard analytical techniques (e.g., Potts & Webb 1992). Loss on ignition (LOI) was determined after igniting 1 g of sample powder in quartz crucibles at 1050°C for 1 hour. Relative analytical uncertainties are estimated to be less than 1% for major elements and between 2% to 5% for trace elements. REEs were measured by ICPMS at the ACME Laboratories in Canada.

Rb, Sr, Sm and Nd, were separated by standard ion exchange liquid chromatography from about 50 mg of whole-rock powder, spiked with mixed ^{84}Sr - ^{87}Rb and ^{150}Nd - ^{149}Sm tracers prior to dissolution in HF acid at 180°C, in pressure digestion bombs. Isotopic composition was measured in static mode on a Finnigan MAT 262 (TIMS) instrument, equipped with 8 Faraday cups. Sr was loaded with a Ta-Hf activator and measured on a single W filament.

Rb was loaded as a chloride and Sm and Nd were loaded as phosphates and measured in double Re-filament configuration mode. The $^{87}\text{Sr}/^{86}\text{Sr}$ ratios were normalized to $^{86}\text{Sr}/^{88}\text{Sr}=0.1194$, the $^{143}\text{Nd}/^{144}\text{Nd}$ ratios to $^{146}\text{Nd}/^{144}\text{Nd}=0.7219$, and Sm isotopic ratios to $^{147}\text{Sm}/^{152}\text{Sm}=0.56081$. Analyses of La Jolla standard gave a mean value of $^{143}\text{Nd}/^{144}\text{Nd}$ ratio = 0.511831 ± 0.000007 (n= 24). NBS 987 Sr standard yielded a $^{87}\text{Sr}/^{86}\text{Sr}$ ratio of 0.710251 ± 0.000008 (n= 34), in good agreement with the certified value (e.g., 0.710248). Total procedural blanks (chemistry and loading) were <160 pg for Sr and <80 pg for Nd. Initial Sr and Nd values were calculated using present-day CHUR values of 0.1967 for $^{147}\text{Sm}/^{144}\text{Nd}$ (Jacobsen & Wasserburg 1980), and 0.512638 for $^{143}\text{Nd}/^{144}\text{Nd}$ (Goldstein *et al.* 1984). Model ages were determined using depleted mantle values as given in Goldstein *et al.* (1984). Decay constants for ^{87}Rb ($1.42 \times 10^{-11} \text{ a}^{-1}$) were taken from Steiger & Jäger (1977), and for ^{147}Sm , ($6.54 \times 10^{-12} \text{ a}^{-1}$) from Lugmair & Marti (1978).

Zircon and titanite were separated from 200–125 mm and 125–63 mm sieved rock fractions by conventional techniques, using the Wilfley Table, magnetic and heavy liquid separation techniques. The internal structure of zircon grains, mounted and polished in epoxy resin, was studied by cathodoluminescence (CL) on a LEO 1459 electron microscope.

For U-Pb isotope dilution analyses, zircon and titanite, washed at room temperature in 6N HCl and 7N HNO_3 and rinsed with ultra clean H_2O , were spiked with mixed ^{205}Pb - ^{235}U spike before dissolution using HF at 205°C in Parr bombs (Parrish 1987). Separation and purification of U and Pb was done in minicolumns with a 40 μl bed of AG1-X8 (100–200 mesh) anion exchange resin in a HBr and HCl medium. U and Pb were loaded with 0.1 N Si gel on single Re filaments and run on MAT 262 TIMS. Pb isotopes were measured in a static collection mode at about 1200°C, while ^{204}Pb was measured on a secondary electron multiplier (SEM), in ion-counting mode. U was analyzed between 1350°C and 1375°C by ion counting. Procedure blanks ranged between 5 and 10 pg for both U and Pb. Fractionation factors for U and Pb correspond to 0.1% per atomic mass unit. Corrections for remaining initial common Pb after the correction for tracer and blank were done

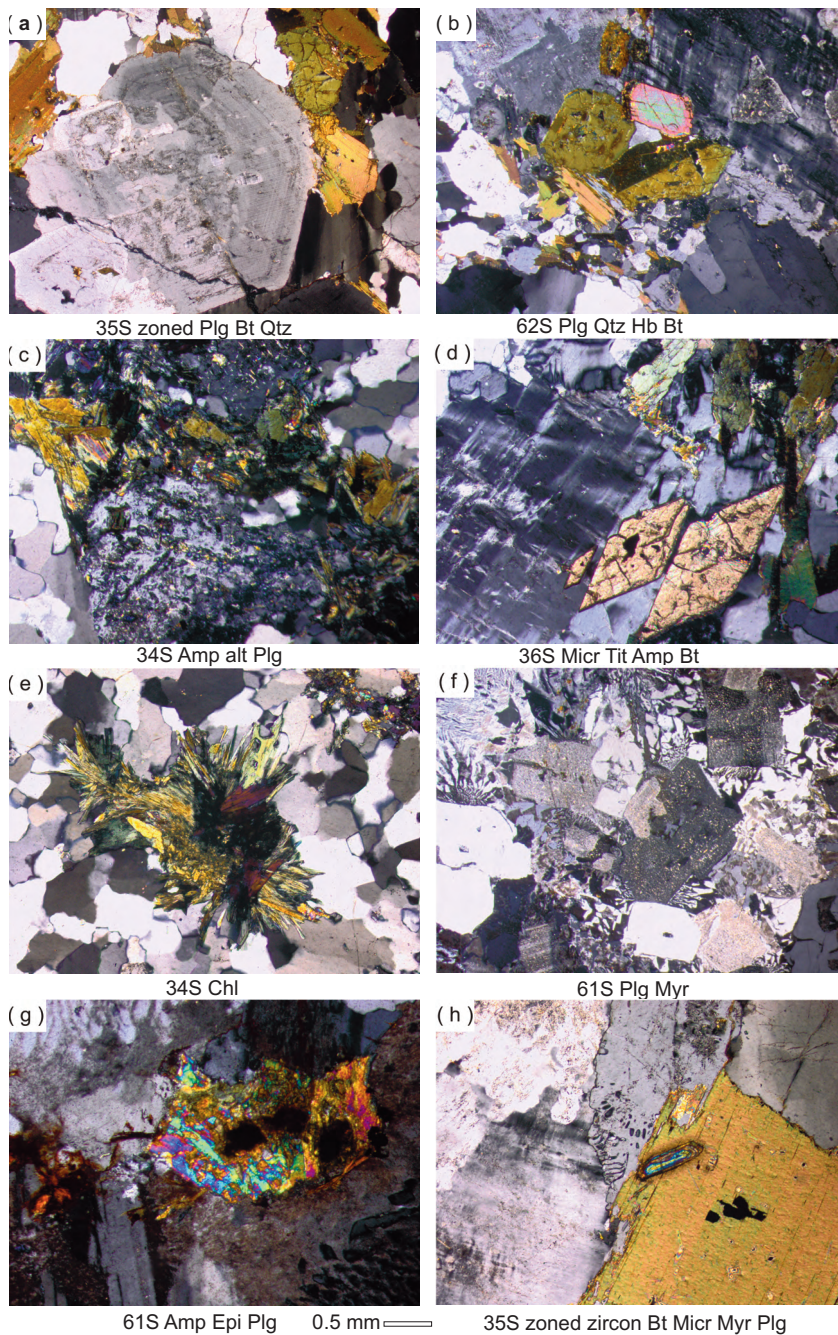


Figure 4. Thin section views under crossed nicols, showing: (a) zoned plagioclase phenocrysts, reddish yellow biotite, green hornblende and quartz; (b) heterogranular texture showing twinned microcline, biotite, antiperthite and quartz; (c) retrograde facies comprising sericitized plagioclase and chloritized biotite and amphibole; (d) euhedral titanite crystal, microcline, biotite and hornblende; (e) chlorite flakes with relict biotite, epidote, mosaic of quartz; (f) myrmekites characterized by quartz-plagioclase intergrowth, K-feldspar, sericitized feldspar; (g) retrograde association of epidote and opaque oxides pseudomorphing hornblende and plagioclase; (h) myrmekite growth at the contact between plagioclase and microcline, reddish yellow biotite and a zircon inclusion in biotite.

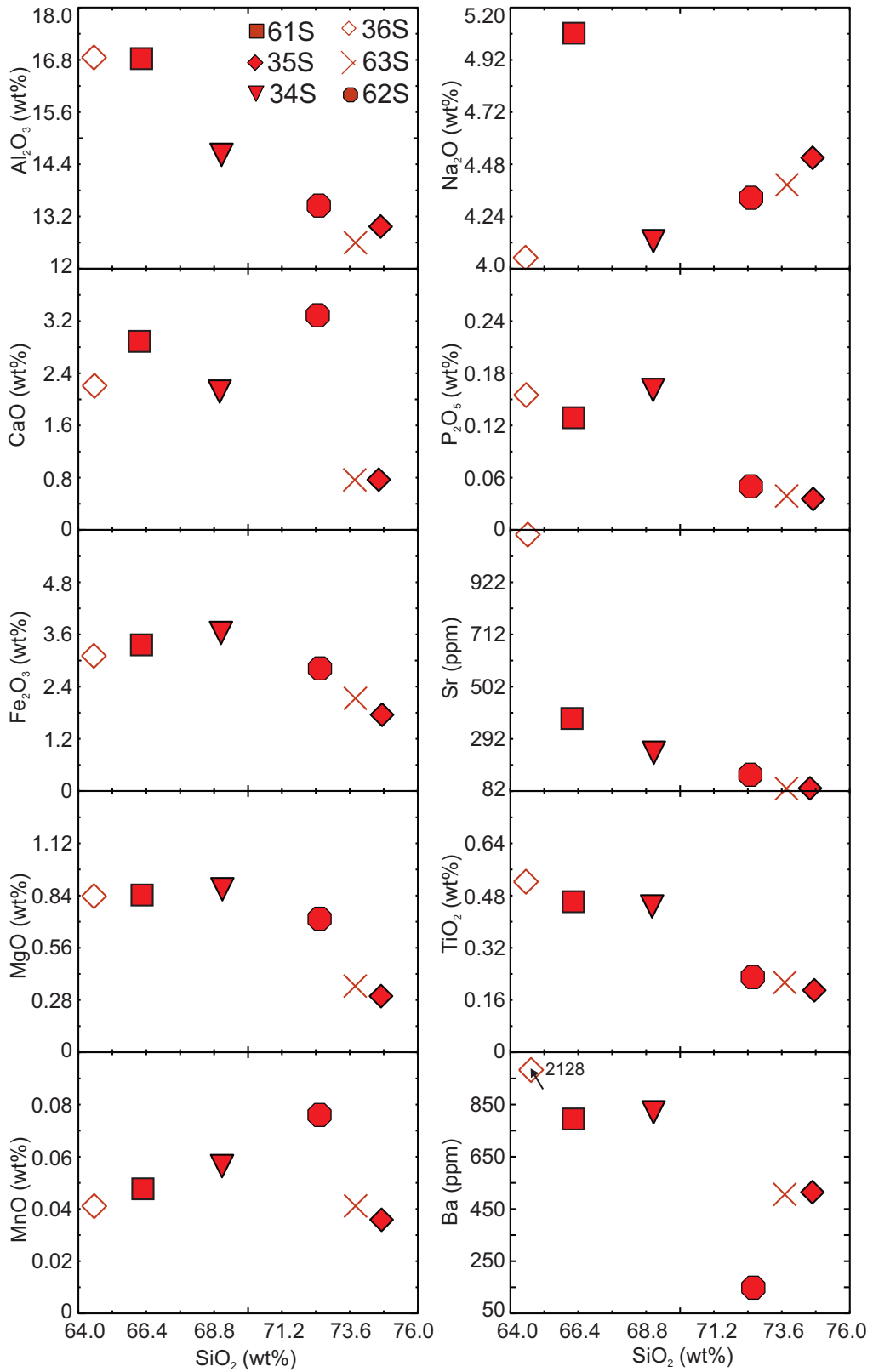


Figure 5. Selected major and trace element Harker diagrams.

following the model of Stacey & Kramers (1975). The U-Pb data were evaluated and plotted using Isoplot version 3.0 from Ludwig (2003).

Results

Geochemistry

Silica content in the analyzed samples ranges between 65 and 75 wt% (Table 1), marking their essentially felsic composition. With the exception of Na₂O, which has a positive correlation trend, and, to some extent MnO, all major elements tend to decrease with increasing SiO₂ (Figure 5, Table 1). The same trend is observed for some trace elements (e.g., Ba, Ga, Sr, V) while the contrary is noted for Co, Ni, Ta, and W (Table 1). The behaviour of the elements with silica variation suggests a pattern consistent with alkali feldspar and plagioclase fractionation in association with amphibole and/or minor clinopyroxene fractionation. In the normative QAP classification diagram (Figure 6a), the analyzed samples plot in the tonalite, granodiorite and monzogranite fields, while one sample plots in the quartz monzonite field. Tonalitic composition is confirmed for one sample on the An-Ab-Or diagram (Figure 6b), while one sample shows the composition of trondhjemite and four are typically granitic.

Alumina Saturation Index, ASI (expressed as molar $A/CNK = [Al_2O_3 / (CaO + Na_2O + K_2O) \text{ mol}\%]$), varies from 0.98 to 1.00, showing a metaluminous composition for the analyzed samples (Table 1, Figure 6d). However, a recalculation taking the P₂O₅ content in apatite into account [$Al_2O_3 / (CaO - 3.3 * P_2O_5 + Na_2O + K_2O) \text{ mol}\%]$), results in slightly higher ASI values with three of the samples showing weakly peraluminous compositions of 1.02 (Table 1). The ASI values below 1.1 point to the I-type character (e.g., White & Chappell 1977) of the analyzed samples. Plots on the SiO₂-K₂O diagram (Figure 6e) mark the high-K composition of most samples, while the lone tonalitic sample has low K and the quartz monzonite sample is characterized by typical shoshonitic composition. Total alkali contents (Na₂O+K₂O) vary from 7.8 to 9.8 wt%, but the most altered sample (34S) unsurprisingly has a very low content of 4.9 wt%. However, plotting the alkalis with FeO and MgO in the AFM diagram (Figure

Table 1. Whole-rock geochemical data; major elements in wt% and trace elements in ppm.

Sample	36S	62S	35S	34S	63S	61S
SiO ₂	64.55	66.24	69.05	72.51	73.78	74.69
TiO ₂	0.52	0.47	0.46	0.23	0.21	0.20
Al ₂ O ₃	16.85	16.82	14.58	13.46	12.60	12.98
Fe ₂ O ₃	3.10	3.38	3.66	2.82	2.13	1.74
MnO	0.04	0.05	0.06	0.08	0.04	0.04
MgO	0.84	0.85	0.89	0.71	0.35	0.31
CaO	2.21	2.90	2.16	3.27	0.77	0.75
Na ₂ O	4.05	5.09	4.13	4.33	4.39	4.51
K ₂ O	5.77	2.93	3.66	0.59	3.98	3.97
P ₂ O ₅	0.16	0.13	0.17	0.05	0.04	0.04
LOI	0.87	0.52	0.51	0.92	0.22	0.36
Sum%	99.29	99.53	99.52	99.03	98.62	99.68
Mg#	35	33	32	33	24	26
ASI	1.00	1.00	0.99	0.98	0.98	0.99
ASI (P ₂ O ₅)	1.02	1.02	1.02	0.99	0.98	1.00
An	13.2	18.0	14.4	26.9	4.5	5.0
Ti+Fe+Mg	4.5	4.7	5.0	3.8	2.7	2.3
Na/K	0.70	1.74	1.13	7.3	1.10	1.14
Fe/Fe+Mg	0.79	0.80	0.80	0.80	0.86	0.85
Na+k	9.82	8.02	7.79	4.92	8.37	8.48
Na+k-Ca	7.6	5.1	5.6	1.7	7.6	7.7
Ba	2128	772	822	116	508	515
Be	5	3	2	0.4		3
Co	69	68	74	103	96	106
Cr	2	6	9	10	9	2
Cs	0.8	1.6	2.6	0.4		0.6
Ga	18.6	22	20	12.6		17.6
Hf	7.9	5.8	7	3.5		5.6
K	47879	24319	30378	4897	32287	32951
Nb	9.6	6.6	8.8	2	19	13.7
Ni	7	25	34	19	13	30
Rb	139	68	90	9	73	71
Sn	2	2	4	0.4		3
Sr	1130.7	380.8	255.2	154.4	83	89.1
Ta	0.9	1.1	1.5	1.2		2.1
Th	8.8	5.2	11.9	0.4		7.3
U	2.6	2.3	5.5	0.2		2.8
V	54	34	32	29	10	12
W	415.4	592.6	681.9	987		879.9
Y	15	22	28	11	35	29
Zn	96	44	83	0	27	0
Zr	282	222	263	130	207	177
K/Rb	344.5	357.6	337.5	544.1	442.3	464.1
Sr/Y	75.4	17.3	9.11	14.0	2.4	3.1
Rb/Sr	0.12	0.18	0.35	0.06	0.11	0.80
La	35	33	42	4.4	30	30.6
Ce	77.4	61	92.7	10.3	73	66
Pr	8.65	6.69	10.3	1.24		7.15
Nd	32.9	25.4	37	8	25	26.2
Sm	5.4	6.7	5.9	2.1	7.0	5.0
Eu	1.4	1.3	1.2	0.6	0.7	0.6
Gd	3.74	3.62	4.78	1.32		4.06
Tb	0.48	0.57	0.77	0.22		0.72
Dy	2.01	3	3.97	1.47		4.49
Ho	0.35	0.58	0.76	0.31		0.88
Er	0.89	1.62	2.26	1.05		2.66
Tm	0.13	0.24	0.33	0.17		0.44
Lu	0.12	0.21	0.3	0.21		0.44
Yb	1.2	1.9	2.4	1.2	3.4	2.9
ΣREE	169.69	145.83	204.67	32.59	139.1	152.14
Eu/Eu*	0.946	0.802	0.686	1.094	0.392	0.405
La _N /Sm _N	4.077	3.098	4.477	1.318	2.697	3.850
Gd _N /Yb _N	2.516	1.538	1.608	0.889		1.130
La _N /Yb _N	19.669	11.711	11.801	2.472	5.911	7.112

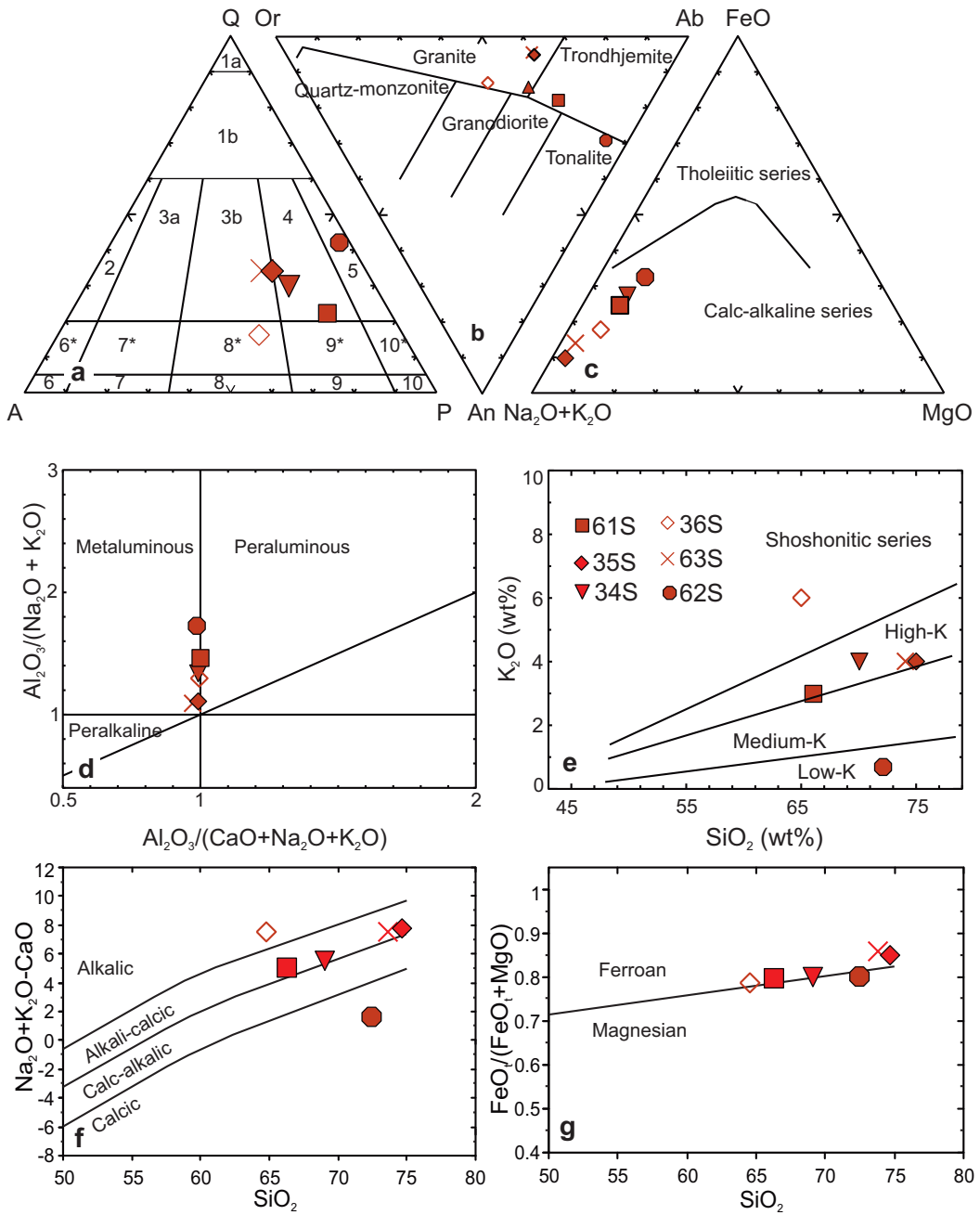


Figure 6. Geochemical diagrams showing classification of samples: (a) the normative quartz-alkali feldspar-plagioclase (QAP) diagram defining various rock types – tonalite (field 5), granodiorite (4), monzogranite (3b) and quartz monzonite (8*); (b) normative albite-anorthite-orthoclase (Ab-An-Or) diagram showing tonalitic, trondhjemitic and granitic affinities of the analyzed samples; (c) (Na₂O+K₂O–FeO–MgO (AFM) diagram showing the calc-alkaline affinity of the analyzed samples; (d) Al₂O₃/(CaO+Na₂O+K₂O) versus Al₂O₃/(Na₂O+K₂O) diagram showing the marginal metaluminous composition of the samples; (e) SiO₂ versus K₂O diagram showing the high-K character of most samples, with a low-K and a shoshonitic sample; (f) SiO₂ versus Na₂O+K₂O–CaO diagram. Most of the samples show alkali-calcic composition. The low-K sample is calcic while the shoshonitic sample shows an alkaline composition; (g) SiO₂ versus FeO/(FeO+MgO) diagram. While three samples are marginally ferroan, one is marginally magnesian and two are clearly ferroan.

6c) still defines the expected differentiation suite (calc-alkaline affinity) for the analyzed samples. The plot of SiO_2 (wt%) versus $\text{Na}_2\text{O}+\text{K}_2\text{O}-\text{CaO}$ (wt%) (Figure 6f) shows alkali-calcic composition for the four high-K samples, an alkaline composition for the shoshonitic sample and a calcic composition for the low-K sample.

The analyzed samples are also distinguished by their mafic element chemistry. Mg\# [$\text{Mg}^{2+}/(\text{Mg}^{2+} + \text{Fe}_{\text{Total}}) \times 100$, with Fe_{Total} as Fe^{2+}] values vary from 24 to 35 (Table 1). Plots in the $\text{SiO}_2-\text{FeO}_t/(\text{FeO}_t+\text{MgO})$ discriminatory diagram (Figure 6g) shows positive correlation, defining a clear ferroan character for two samples, a marginal ferroan one for three others and a marginal magnesian composition for the tonalitic sample.

Primitive mantle normalized trace element spidergrams show three groups of samples. Group one (tonalite 62S and quartz monzonite 36S; Figure 7a) is marked by relatively high Sr, Rb and Ba contents and a high Sr/Y ratio (Table 1), as well as low Dy, Y, Er, Yb and Lu contents compared to group two (trondhjemitite 61S and two monzogranites 35S and 63S; Figure 7b), that is also distinguished by a negative Sr anomaly. The lone sample (granodiorite 34S; Figure 7c) is clearly distinguished from the others by its general low trace element abundance and its K peak. Otherwise, all the samples show Nb and Ti negative anomalies similar to chemical features observed in subduction-related rocks.

Chondrite-normalized REE patterns (Figure 8) also distinguish the three groups identified in the trace element spidergrams. Group one samples show similarities with Archaean TTG REE patterns (e.g., figure 8a in Martin 1987) and are enriched in LREE and markedly depleted in HREE ($\text{La}_N/\text{Yb}_N = 19.7$ and 11.7) relative to chondrites. They have slight negative Eu anomalies ($\text{Eu}/\text{Eu}^* = 0.946, 0.802$). Like Archaean TTGs, sample 36S in particular is strongly depleted in HREE ($\text{Gd}_N/\text{Yb}_N = 2.52$; $\text{La}_N/\text{Yb}_N = 19.67$) compared to chondrites. Group two samples, however, are different from Archaean TTGs, and are more like post-Archaean granitoids (Figure 8b; Graviou 1984 in Martin 1993). They have strong negative Eu anomalies ($\text{Eu}/\text{Eu}^* = 0.39$ to 0.69). Sample 61S is less depleted in HREE ($\text{Gd}_N/\text{Yb}_N = 1.13$, $\text{La}_N/\text{Yb}_N = 7.11$). The lone group three sample with the lowest overall abundance in REE is very depleted in LREE

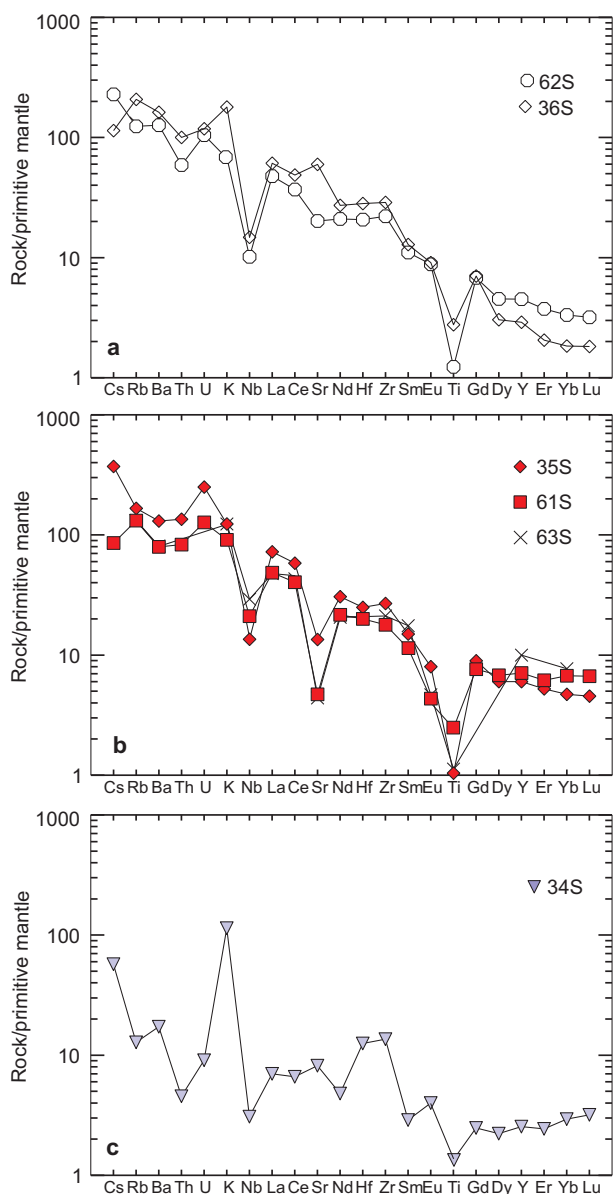


Figure 7. Primitive mantle normalized trace element spidergrams: (a) samples 62S and 36S are marked by relatively high Sr, Rb and Ba contents and low Dy, Y, Er, Yb and Lu contents compared to samples 61S, 35S, and 63S (b); (c) sample 34S is marked by general low trace element abundance and a high K peak.

and enriched in HREE ($\text{La}_N/\text{Yb}_N = 2.47$) relative to chondrites and has a positive Eu anomaly (Figure 8c).

Geochronology

Zircon Cathodoluminescence (CL) and Zircon U-Pb Ages – Three zircon populations characterized by

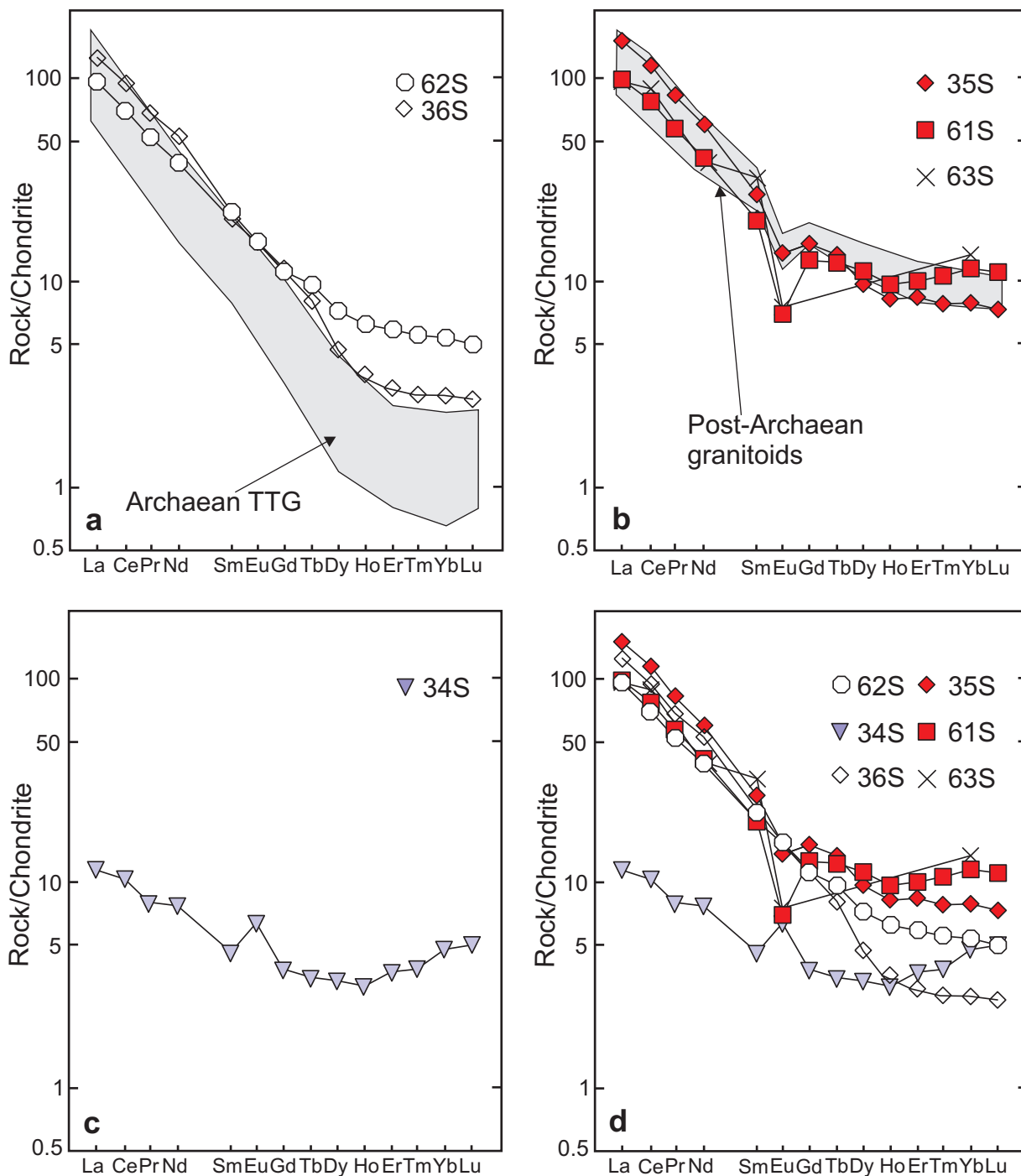


Figure 8. Chondrite normalized REE patterns, normalization according to Boynton (1984); (a) sample 36S and 62S REE patterns compared with Archaean TTG patterns (e.g., Martin 1987 in Martin 1993); (b) sample 35S, 61S and 63S REE patterns compared with post-Archaean granitoid REE patterns (e.g., Graviou 1984 in Martin 1993); (c) sample 34S showing depleted LREE and a relatively enriched HREE pattern compared to Archaean TTG relative to chondrite; (d) comparison of the three different patterns shown in (a), (b), and (c).

idiomorphic crystals with plane faces and sharp edges (a, b, c), and one population with slightly abraded crystals (d) were identified in the studied samples: (a) thick, prismatic, reddish-yellow; (b) medium, long, prismatic, colourless; (c) thick, prismatic, yellow; (d) medium to small, octahedral-globular, smoky-dark. All zircons have oscillatory zoning (Figure 9) typical of a magmatic origin. They were analyzed for U-Pb age determination (Table 2). Each fraction was made of a single zircon grain.

The reddish yellow grains were separated from samples 35S and 62S. Twelve zircon fractions from 35S and six from 62S give dissimilar and discordant $^{207}\text{Pb}/^{235}\text{U}$ and $^{206}\text{Pb}/^{238}\text{U}$ ratios that define discordias with identical upper intercept ages of 631 ± 3.8 Ma and 638.3 ± 5.7 Ma, respectively (Figure 10a, b). Despite its similar Neoproterozoic apparent $^{207}\text{Pb}/^{206}\text{Pb}$ age with discordia upper intercept ages, fraction 35S-4c gives Early Proterozoic $^{207}\text{Pb}/^{235}\text{U}$ apparent age and late Archaean $^{206}\text{Pb}/^{238}\text{U}$ apparent age (Table 2).

Five fractions analyzed from the colourless zircon population separated from sample 35S are also discordant, yielding a younger upper intercept age (607 ± 10 Ma) than that from the reddish yellow zircon fractions (Figure 10c).

The typical yellow zircon population characterizes samples 63S, 34S and 61S. They all give dissimilar and discordant $^{207}\text{Pb}/^{235}\text{U}$ and $^{206}\text{Pb}/^{238}\text{U}$ ratios, defining discordia with similar upper intercept ages within error of 728 ± 11 Ma, 717 ± 24 Ma, and 702 ± 34 Ma (Figure 10d–f).

Two extreme ages, the youngest obtained from two fractions of the colourless zircon population from sample 35S and the oldest from six fractions of smoky zircon population from sample 34S were obtained. One fraction from the colourless zircons is concordant giving the youngest zircon age of 554.2 ± 2.1 Ma (Figure 11a). A two-point discordia with the slightly positively discordant fraction gives an intercept age of 556 ± 7.9 Ma, identical with the age of the concordant fraction. Four of the six fractions from smoky zircons give discordia with an Archaean upper intercept age of 3025 ± 380 Ma and a Neoproterozoic lower intercept age of 602 ± 350 Ma (Figure 11b) similar to the age of the colourless zircon population. Apparent $^{207}\text{Pb}/^{235}\text{U}$ and $^{206}\text{Pb}/^{238}\text{U}$

ages from the smoky zircon population fractions range from Neoproterozoic to Early Proterozoic (587–2095 Ma), while the $^{207}\text{Pb}/^{206}\text{Pb}$ apparent ages are Early Proterozoic to Late Archaean (1777–2821 Ma; Table 2).

Titanite U-Pb Ages – Eight titanite fractions from sample 34S, six from sample 35S, six from sample 62S and four from sample 63S were analyzed for U-Pb age determination (Table 3).

Of the eight fractions from sample 34S, six gave concordant $^{207}\text{Pb}/^{235}\text{U}$ and $^{206}\text{Pb}/^{238}\text{U}$ ratios with mean ages ranging from 671 ± 11 Ma to 599.5 ± 7.1 Ma. The weighted mean of four identical $^{206}\text{Pb}/^{238}\text{U}$ apparent ages is 607 ± 10 Ma (Figure 12a), being indistinguishable from the age of the colourless zircon population. The titanite ages are younger than the zircon ages of 717 ± 24 Ma, and 3035 ± 380 Ma from the same sample, but similar to the lower intercept age (602 ± 350 Ma; Figure 11b) from the Archaean smoky zircon fractions.

Five titanite fractions from sample 35S and five from sample 62S are concordant but one fraction from each sample is slightly discordant (Figure 12b, c). The mean of the $^{207}\text{Pb}/^{235}\text{U}$ and $^{206}\text{Pb}/^{238}\text{U}$ apparent ages from sample 35S ranges from 657.5 ± 5.2 Ma to 545.9 ± 5.3 Ma, giving an overall weighted mean age of 600 ± 29 Ma (Figure 12b). These ages are younger than or closely conform to zircon ages from the same sample. The oldest $^{207}\text{Pb}/^{235}\text{U}$ and $^{206}\text{Pb}/^{238}\text{U}$ apparent ages from three fractions from sample 62S give a weighted mean age of 606 ± 10 Ma (Figure 12c). A similar intercept age within error of 612 ± 28 Ma was obtained from the lone discordant fraction. These titanite U-Pb ages from sample 62S are identical with the $^{207}\text{Pb}/^{206}\text{Pb}$ apparent ages that range from 621.5 to 598.4 (Table 3). The titanite ages for sample 62S are only slightly younger than the zircon age of 638.3 ± 5.7 Ma from the same sample.

Four fractions from sample 63S are dispersed along the concordia (Figure 12d). Their $^{207}\text{Pb}/^{235}\text{U}$ and $^{206}\text{Pb}/^{238}\text{U}$ apparent ages vary between 612.6 and 372.9 Ma. The oldest mean age of 596 ± 12 Ma is similar to titanite ages from other samples, but more than 100 My younger than the 728 ± 11 Ma zircon age from the same sample.



Figure 9. Cathodoluminescence (CL) images portraying regular oscillatory magmatic zoning of representative zircons. Notice fractures and pores that probably mark fluid and Pb-loss paths.

Table 2. Zircon U-Pb analytical data corrected for common Pb according to the two stage evolution model of Stacey & Kramers (1975).

Sample/ Sample fraction	Sample weight in mg	²⁰⁶ Pb ²⁰⁴ Pb	U (ppm)	Pb (ppm)	Pb _{rad} (ppm)	Pb _{com} (ppm)	Pb _{com} in %	Atomic ratios				calculated apparent ages (Ma)			
								²⁰⁶ Pb* ²⁰⁶ Pb*	²⁰⁶ Pb ²³⁸ U	²⁰⁷ Pb ²³⁵ U	Correlation coefficient	²⁰⁶ Pb* ²⁰⁶ Pb*	²⁰⁶ Pb* ²³⁸ U	²⁰⁷ Pb* ²³⁵ U	²⁰⁷ Pb* ²⁰⁶ Pb*
34S Archaean															
34S-1	0.0141	26.45	697.7	549.8	-	-	-	0.200393	0.09528±234	1.4276±4910	0.41	0.10867±3640	586.7	900.6	1777.2
34S-4	0.0189	345.1	722.1	270.5	243.9	26.6	9.83	0.509867	0.23239±128	5.6472±0319	0.98	0.17625±0021	1347.0	1923.3	2617.9
34S-4B	0.0189	345.1	723.1	270.5	239.3	31.2	11.5	0.503087	0.22881±123	5.5223±0309	0.97	0.17504±0217	1328.3	1904.1	2606.5
34S-1A	0.0116	363.5	363.8	153.4	138.6	14.8	9.65	0.484108	0.27063±203	6.8717±0566	0.93	0.18416±0054	1544.0	2095.0	2690.7
34S-2A	0.0190	93.63	220.2	94.58	65.08	29.5	31.2	0.514697	0.20477±146	4.5262±0406	0.84	0.16031±0077	1200.9	1735.8	2458.9
34S-10C	0.0125	30.27	2.893	4.422	-	-	-	0.684879	0.17355±191	4.7706±4112	0.41	0.19937±1638	1031.6	1779.7	2821.0
34S Pan-African															
34S-1	0.0162	453.9	96.77	14.4	12.64	1.76	12.2	0.121076	0.12831±241	1.1309±668	0.46	0.06393±339	778.2	768.2	739.2
34S-2	0.0217	5343.4	175.1	18.3	18.09	0.21	1.14	0.087565	0.10422±086	0.9208±189	0.50	0.06408±115	639.1	662.8	744.2
34S-3	0.0196	715.3	193.9	21.7	19.95	1.75	8.06	0.107207	0.10206±110	0.8838±278	0.47	0.06280±176	626.5	643.0	701.6
34S-4	0.0186	12584.0	216.2	17.8	17.79	0.01	0.06	0.064866	0.08466±076	0.7249±177	0.48	0.06210±134	523.9	553.6	677.5
34S-5	0.0140	2725.7	78.92	9.10	08.9	0.20	2.19	0.105681	0.11225±346	0.9689±951	0.45	0.06259±554	687.9	687.9	694.6
34S-6	0.0146	338.9	144.1	11.5	9.64	1.86	16.1	0.094537	0.06738±175	0.5862±498	0.46	0.06310±484	420.4	468.5	711.5
34S-7	0.0104	732.1	156.4	13.0	12.0	1.04	8.00	0.091329	0.07725±231	0.6760±658	0.45	0.06347±558	479.7	524.4	723.9
34S-8	0.0091	1908.3	185.1	18.1	17.5	0.59	3.26	0.107053	0.09689±227	0.8504±622	0.46	0.06366±418	596.2	624.9	730.3
34S-9	0.0121	4480.6	234.7	21.0	20.7	0.28	1.33	0.143987	0.08521±139	0.7254±369	0.45	0.06174±283	527.2	553.9	665.2
34S-10	0.0185	3828	77.43	9.08	8.93	0.15	1.65	0.100244	0.11535±268	1.0221±733	0.46	0.06427±412	703.7	715.0	750.5
34S-11	0.0167	4877.4	86.61	10.3	10.13	0.13	1.26	0.099432	0.11700±276	1.0213±730	0.47	0.06331±405	713.2	714.6	718.8
34S-12	0.0152	1032	2022.7	37.7	35.5	2.19	5.81	0.083176	0.01786±015	0.1506±347	0.48	0.06114±124	114.1	142.4	644.2
35S Pan-African															
35S-1	0.0174	3515.7	3436.1	234.8	230.5	4.32	1.84	0.034485	0.07123±041	0.5976±038	0.91	0.06083±016	443.6	475.6	633.4
35S-1B	0.0174	3463.9	3436.1	234.8	230.4	4.38	1.86	0.034848	0.07119±041	0.5986±384	0.91	0.06099±016	443.3	476.4	638.8
35S-2	0.0249	2385.1	978.3	84.81	82.56	2.24	2.64	0.055576	0.08793±048	0.7374±576	0.74	0.06082±032	543.3	560.9	632.9
35S-3	0.0143	1856.3	1274.5	110.2	106.4	3.77	0.03	0.043383	0.08803±053	0.7348±701	0.67	0.06054±043	543.9	559.4	622.9
35S-4	0.0122	552.5	3858.6	66.61	59.46	7.15	10.7	0.055113	0.01606±011	0.1349±232	0.51	0.06091±091	102.7	128.5	636.0
35S-5	0.0188	982.5	4294.7	96.60	90.50	6.10	6.32	0.043286	0.02221±014	0.1856±169	0.72	0.06065±038	141.6	173.0	626.8
35S-6	0.0314	436.0	259.5	28.96	25.41	3.55	12.2	0.166571	0.09286±067	0.7518±133	0.50	0.05871±091	571.5	569.3	556.4
35S-7	0.0170	215.0	373.9	47.80	37.30	10.5	21.9	0.230477	0.08989±071	0.7251±167	0.47	0.05851±121	554.9	553.7	548.8
35S-1C	0.0108	7098.3	647.9	61.19	60.7	0.49	0.80	0.192375	0.08692±059	0.7199±107	0.54	0.06007±075	537.3	550.7	606.4
35S-2C	0.0268	1004.0	347.5	35.69	33.75	1.94	5.43	0.209488	0.08887±062	0.7352±188	0.52	0.06000±083	548.9	559.6	603.5
35S-3C	0.0153	9541.4	366.6	38.33	38.10	0.23	0.60	0.207878	0.09522±061	0.7894±939	0.60	0.06013±057	586.4	590.9	608.3
35S-4C	0.0202	1355.8	469.5	268.1	255.7	12.4	4.62	0.051422	0.53857±293	4.5039±265	0.93	0.06065±013	2777.5	1731.7	626.9
35S-5C	0.0184	7494.8	267.1	26.22	26.02	0.20	0.76	0.190927	0.09052±072	0.7443±147	0.50	0.05963±103	558.6	564.9	590.3
35S-6C	0.0426	2589.7	453.6	42.75	44.82	0.93	2.17	0.199316	0.08506±060	0.7039±718	0.73	0.06002±042	526.3	541.1	604.1
35S-7R	0.0305	3594.0	1858	142.7	140.2	2.54	1.78	0.047887	0.07914±043	0.6628±403	0.91	0.06074±015	491.0	516.3	630.0
35S-8R	0.0458	3563.5	3774.5	22.82	22.47	0.35	1.53	0.231497	0.00535±004	0.0443±065	0.54	0.06001±074	34.40	44.00	603.9
35S-9R	0.0235	3519.4	1384.7	106.4	104.5	1.93	1.81	0.051348	0.07889±043	0.6600±047	0.79	0.06068±027	489.5	514.6	627.8
35S-10R	0.0258	488.3	1902.4	103.9	91.50	12.4	11.9	0.060117	0.04990±040	0.4149±395	0.87	0.06030±028	413.9	352.4	614.6
35S-11R	0.0333	1582.9	3121.7	176.4	169.4	7.02	3.97	0.045518	0.05705±034	0.4780±305	0.95	0.06077±012	357.7	396.7	631.0
35S-12R	0.0277	3410.0	5689.0	279.0	273.8	5.20	1.86	0.053588	0.05024±028	0.4201±247	0.97	0.06064±009	316.0	356.2	626.7

Table 2. Continued.

Sample/ Sample fraction	Sample weight in mg	²⁰⁹ Pb	U (ppm)	Pb (ppm)	Pb _{rad} (ppm)	Pb _{com} (ppm)	Pb _{com} in %	²⁰⁸ Pb* _{208Pb*}	²⁰⁶ Pb _{238U}	²⁰⁷ Pb _{235U}	Correlation coefficient	²⁰⁷ Pb* _{206Pb*}	²⁰⁶ Pb* _{238U}	²⁰⁷ Pb* _{235U}	²⁰⁷ Pb* _{206Pb*}
61S Pan-African															
61S-1	0.0168	45.15	1079.8	25.56	7.66	17.9	70.0	0.099699	0.00731±08	0.0343±037	0.21	0.03403±364	46.95	34.24	-
61S-2	0.0186	268.9	974.1	74.60	60.5	14.1	18.9	0.169544	0.05888±062	0.4579±094	0.57	0.05640±096	368.8	382.8	468.3
61S-3	0.0217	4632.8	206.0	22.52	22.23	0.29	1.29	0.125163	0.10559±078	0.9122±162	0.51	0.06266±096	647.1	658.2	696.7
61S-4	0.0184	4801.0	172.67	15.95	15.75	0.20	1.25	0.127921	0.08921±128	0.7517±330	0.46	0.06111±241	550.9	569.2	643.1
61S-5	0.0110	4260.1	335.0	32.00	31.55	0.45	1.40	0.132123	0.09185±112	0.7818±286	0.47	0.06173±202	566.5	586.5	664.8
61S-6	0.0137	1541.7	241.7	28.71	27.61	1.10	3.83	0.132117	0.11124±083	0.9525±167	0.52	0.06210±093	679.9	679.4	677.6
62S Pan-African															
62S-1	0.0339	4615	1060	82.67	81.51	1.16	1.40	0.044316	0.08094±045	0.6794±047	0.83	0.06088±024	501.7	526.4	634.9
62S-2	0.0414	3578.7	6027.5	149.6	146.9	2.71	1.81	0.037418	0.02581±015	0.2167±013	0.96	0.06088±011	164.3	199.1	634.9
62S-3	0.0198	2570.9	1205.6	98.82	96.37	2.45	2.47	0.050348	0.08366±047	0.7043±057	0.72	0.06106±034	517.9	541.4	641.4
62S-4	0.0221	3058.3	1081.9	89.89	88.01	1.88	2.01	0.051064	0.08510±047	0.7142±057	0.73	0.05609±034	526.5	547.2	634.7
62S-5	0.0155	3077.9	2493.9	101.8	99.66	2.14	2.10	0.040101	0.04221±024	0.3551±033	0.67	0.06101±042	266.5	308.5	639.7
62S-6	0.0211	2091.9	1737.2	107.7	104.4	3.26	3.03	0.055416	0.06263±034	0.5276±039	0.75	0.06109±030	391.6	430.2	642.5
63S Pan-African															
63S-1	0.0166	487.18	253.63	33.26	29.57	3.69	11.1	0.159811	0.11071±104	0.9773±253	0.83	0.06403±147	676.9	692.2	742.4
63S-2	0.0138	308.39	373.64	45.35	37.56	7.79	17.2	0.125791	0.09821±086	0.8716±207	0.49	0.06437±135	603.9	636.5	753.8
63S-3	0.0119	1009.9	1188.8	175.5	166.0	9.46	5.39	0.205189	0.12795±072	1.1204±095	0.71	0.06351±038	776.2	763.2	725.3
63S-4	0.0123	586.19	1133.8	89.54	80.83	8.71	9.73	0.107749	0.07076±045	0.6212±081	0.56	0.06367±069	440.7	490.6	730.8
63S-5	0.0118	304.80	341.03	32.33	26.87	5.46	16.9	0.163474	0.07457±096	0.6615±261	0.47	0.06434±228	463.6	515.5	752.8
63S-6	0.0129	91.857	1.1453	86.13	48.13	38.0	44.1	0.157784	-	-	-	0.06685±120	-	-	833.3

All errors quoted are 2σ absolute uncertainties and refer to the last digit.
* - radiogenic; grain size varies from 80–225 μm

Table 3. Titanite U-Pb analytical data corrected for common Pb according to the two stage evolution model of Stacey & Kramers (1975).

Sample/ Sample fraction	Sample weight in mg	²⁰⁶ Pb ²⁰⁶ Pb	U (ppm)	Pb (ppm)	Pb _{rad} (ppm)	Pb _{com} (ppm)	Pb _{com} in %	Atomic ratios				calculated apparent ages (Ma)			
								²⁰⁸ Pb* ²⁰⁶ Pb*	²⁰⁶ Pb ²³⁸ U	²⁰⁷ Pb ²³⁵ U	Correlation coefficient	²⁰⁷ Pb* ²⁰⁶ Pb*	²⁰⁶ Pb* ²³⁸ U	²⁰⁷ Pb* ²³⁵ U	²⁰⁷ Pb* ²⁰⁶ Pb*
34S															
34S-1	0.0166	1385.1	209.99	25.08	24.13	0.95	3.78	0.282696	0.09942±119	0.8151±302	0.46	0.05946±198	611.0	605.3	584.1
34S-2	0.0176	13601	112.35	13.63	13.58	0.05	0.37	0.292033	0.10369±206	0.8822±573	0.43	0.06171±354	636.0	642.2	664.0
34S-3	0.0156	1145.7	216.3	25.27	24.11	1.16	4.59	0.268895	0.09743±124	0.8083±320	0.44	0.06017±215	599.3	601.5	609.8
34S-4	0.0260	760.66	120.5	15.76	14.75	1.01	6.41	0.356026	0.10078±179	0.7429±397	0.42	0.05347±259	619.0	564.1	348.7
34S-5	0.0172	1221.4	185.75	21.04	20.08	0.96	4.56	0.202783	0.09964±129	0.8025±331	0.45	0.05841±218	612.3	598.2	545.1
34S-6	0.0269	2559.8	78.25	9.45	9.25	0.20	2.12	0.235681	0.10582±189	0.9018±509	0.45	0.06181±315	648.4	652.7	667.5
34S-7	0.0091	496.68	216.4	27.47	24.71	2.76	10.0	0.285331	0.09821±242	0.8837±737	0.38	0.06527±505	603.9	643.0	783.0
34S-8	0.0102	1164.5	211.6	26.21	24.95	1.26	4.81	0.186256	0.10988±195	0.9177±488	0.46	0.06057±289	672.1	661.1	624.0
35S															
35S-1	0.0245	675.09	210.79	27.21	25.08	2.13	7.82	0.223802	0.10767±091	0.8875±207	0.48	0.05978±123	659.2	645.0	595.6
35S-2	0.0314	583.21	172.89	20.48	18.73	1.75	8.54	0.303791	0.09229±410	0.7552±394	0.86	0.05935±157	569.1	571.2	579.9
35S-3	0.0291	842.56	181.92	21.63	20.25	1.38	6.38	0.220526	0.10100±156	0.8276±228	0.62	0.05943±130	620.3	612.3	582.9
35S-4	0.0292	807.14	210.39	21.52	20.06	1.46	6.78	0.196829	0.08819±091	0.7228±180	0.51	0.05944±128	544.8	552.3	583.3
35S-5	0.0306	847.5	165.74	20.33	19.14	1.19	5.85	0.334426	0.09620±094	0.7822±212	0.47	0.05898±142	592.1	586.8	566.2
35S-6	0.0367	997.56	92.81	11.47	10.89	0.58	5.06	0.330121	0.09812±292	0.7958±377	0.68	0.05882±205	603.4	594.5	560.5
62S															
62S-1	0.0356	889.01	153.28	17.92	16.89	1.03	5.75	0.296784	0.09435±369	0.7870±359	0.87	0.06050±135	581.2	589.5	621.5
62S-2	0.0303	623.06	193.58	22.55	20.74	1.81	8.03	0.308061	0.09095±107	0.7506±192	0.54	0.05986±129	561.1	568.6	598.4
62S-3	0.0603	596.75	135.10	17.02	15.60	1.42	8.34	0.309926	0.09786±314	0.8125±288	0.91	0.06022±086	601.9	606.9	611.4
62S-4	0.0284	684.01	170.41	19.91	18.44	1.47	7.38	0.300422	0.09237±227	0.7641±279	0.71	0.05999±154	569.5	576.4	603.5
62S-5	0.0345	820.71	137.40	17.33	16.27	1.06	6.12	0.324166	0.09936±139	0.8237±240	0.56	0.06012±146	610.7	610.1	608.0
62S-6	0.0794	455.09	192.78	21.82	19.43	2.39	10.9	0.280620	0.08731±079	0.7235±093	0.73	0.06010±053	539.6	552.7	607.1
63S															
63S-1	0.0116	92.951	35.94	5.318	3.328	1.99	22.4	0.546299	0.06715±385	0.4823±1230	0.41	0.05209±1234	418.9	399.7	289.7
63S-2	0.0104	306.85	71.88	8.62	7.39	1.23	14.3	0.445425	0.07939±497	0.6374±1389	0.44	0.05823±1158	492.5	500.7	538.4
63S-3	0.0090	4757.4	854.1	101.4	100.3	1.08	1.07	0.356479	0.09610±303	0.8281±499	0.71	0.06250±304	591.5	612.6	691.2
63S-4	0.0086	315.13	187.5	18.88	16.55	2.33	12.3	0.662902	0.05955±475	0.4632±1339	0.44	0.05640±1489	372.9	386.5	468.3

All errors quoted are 2σ absolute uncertainties and refer to the last digit.* - radiogenic; grain size varies from 80–225 μm

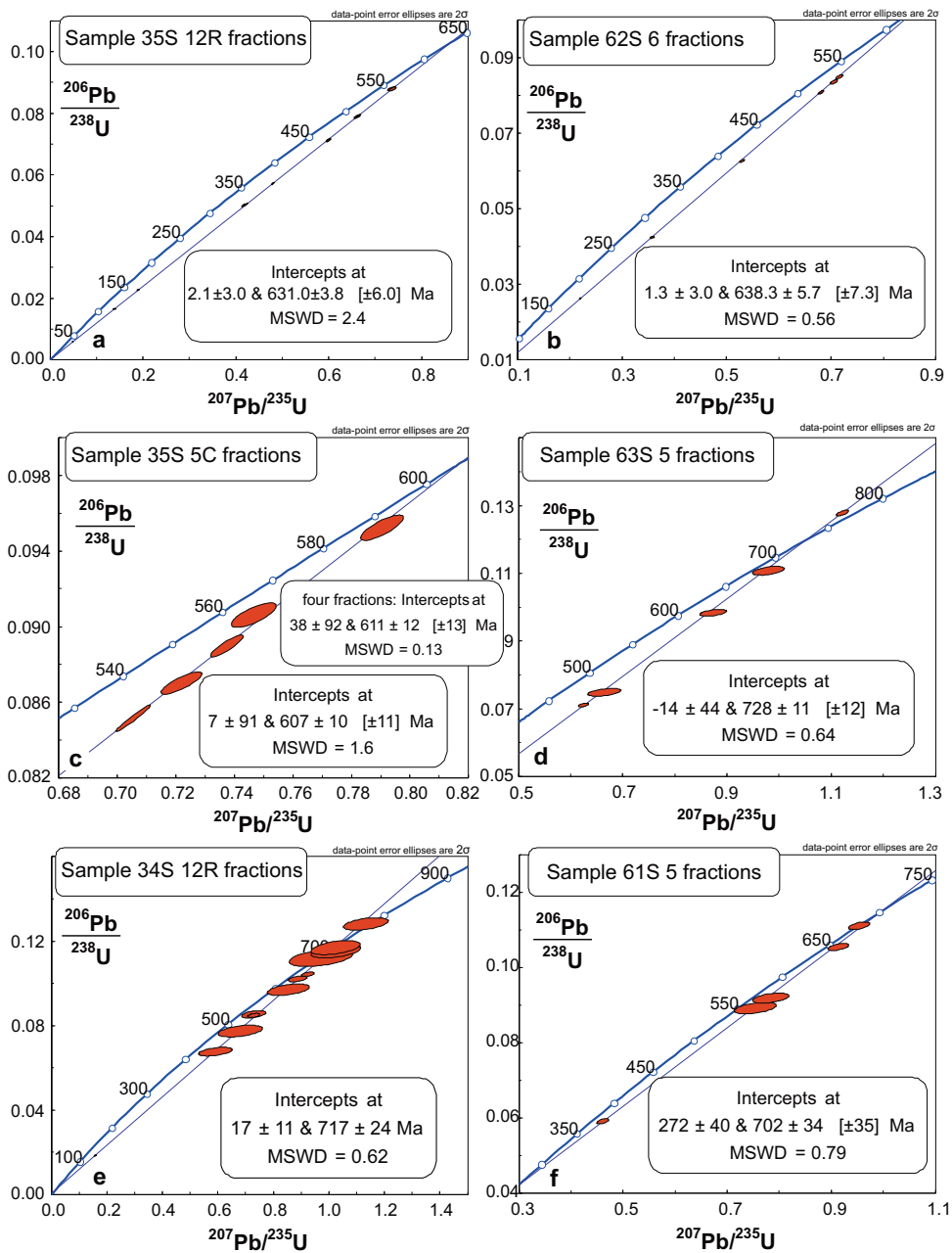


Figure 10. Zircon discordia diagrams of the studied samples: (a) sample 35S discordia for 12 reddish yellow zircon fractions with an upper intercept age of 631 ± 3.8 Ma; (b) a similar upper intercept age of 638.3 ± 5.7 Ma for six fractions of the reddish yellow zircons from sample 62S; (c) five zircon fractions from the colourless zircon population with low degrees of discordance and a younger age of 607 ± 10 Ma compared to the reddish yellow population ages; (d) five fractions of the yellow zircon population from sample 63S; (e) 12 fractions of the yellow zircon population from sample 34S; and (f) five fractions of the yellow zircon population from sample 61S. Upper intercepts in (d), (e), and (f) give similar ages within error of 728 ± 11 Ma, 717 ± 24 Ma and 702 ± 34 Ma, respectively. Notice the low degrees of discordances of the yellow zircon populations compared to the reddish yellow population. Some fractions of 34S (Figure 10e) are even concordant.

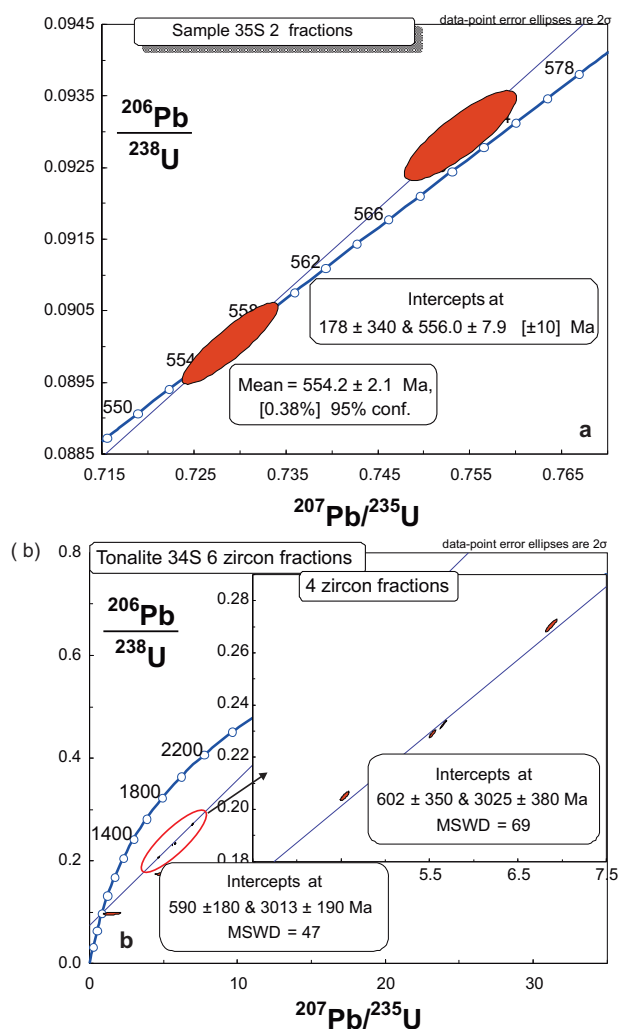


Figure 11. Extreme zircon age data from the analyzed samples: (a) the lone and youngest concordant zircon fraction (554.2 ± 2.1 Ma) from the colourless zircon population from sample 35S and a slightly discordant fraction, both making an intercept age of 556 ± 7.9 Ma; (b) six fractions from the smoky zircon population, all highly discordant and giving an Archaean upper intercept age and a Neoproterozoic lower intercept age. Four aligned fractions give an upper intercept of 3025 ± 380 Ma and a lower intercept of 602 ± 350 Ma.

Sm-Nd and Rb-Sr Systematics

Five samples (34S, 35S, 61S, 62S and 63S) were investigated for whole-rock Sm-Nd and Rb-Sr isotope composition (Table 4). Rb-Sr data yield an errorchron age of 674 ± 46 Ma (five WR, MSWD = 42924, initial $^{87}\text{Sr}/^{86}\text{Sr}$ ratio = 0.7023 ± 0.0011 , Figure 13). Sample 34S and 62S, with low Rb/Sr ratios, lie on the errorchron, while sample 35S, with a high Rb/

Sr ratio, and sample 63S, with the highest one, lie below it. Sample 61S, with the second highest Rb/Sr ratio, lies above the errorchron. Initial $^{87}\text{Sr}/^{86}\text{Sr}$ (Sr_i) ratios calculated for the Neoproterozoic zircon age of ca. 640 Ma give low values ranging from 0.702389 to 0.704011 and similar to the errorchron value. ϵ_{Nd} values obtained are all positive, varying between +5.05 and +8.66. These isotope values indicate the juvenile nature of the source. The model age algorithm (Goldstein *et al.* 1984) gives Nd TDM ages between 653 and 917 Ma, very similar to the zircon ages, except for the Archaean zircon age. This tends to confirm the juvenile nature of the source.

Discussion

Zircon CL and Age Implications

Zircon CL images (Figure 9) show the internal structure of representative zircon grains characterized by oscillatory zoning typical of regular magmatic growth. In addition, their idiomorphic forms tend to suggest that they are all in situ, as opposed to detrital zircon with rounded and xenomorphic forms that indicate polished surfaces due to abrasion during erosion and transportation to their present location. However, the smoky zircon population, now dated as Archaean in age, shows some rounded morphologies, raising doubts about its origin in the analyzed granitoids.

Discordia upper intercept ages are interpreted as zircon crystallization ages. Five zircon crystallization episodes are recorded in this study. Firstly, the 3035 ± 380 Ma Archaean zircon crystallization age (Figure 11b) is interpreted as an inherited age, given that no Nd TDM age in the analyzed samples show such an old age. Secondly, the yellow zircon population whose ages (702 ± 34 Ma to 728 ± 11 Ma; Figure 10d-f) are similar to the age of the Neoproterozoic alkaline magmatism recently reported in the Sudan basement north of the present study area (e.g., Shang *et al.* 2010b) and indicate that the studied granitoid basement north of Delgo record this Neoproterozoic magmatism event even though they are not alkaline. Thirdly, the ca. 630 Ma (631 ± 3.8 Ma and 638.3 ± 5.7 Ma; Figure 10a, b) ages of the reddish-yellow zircon population are interpreted to mark the beginning of the tectono-thermal and

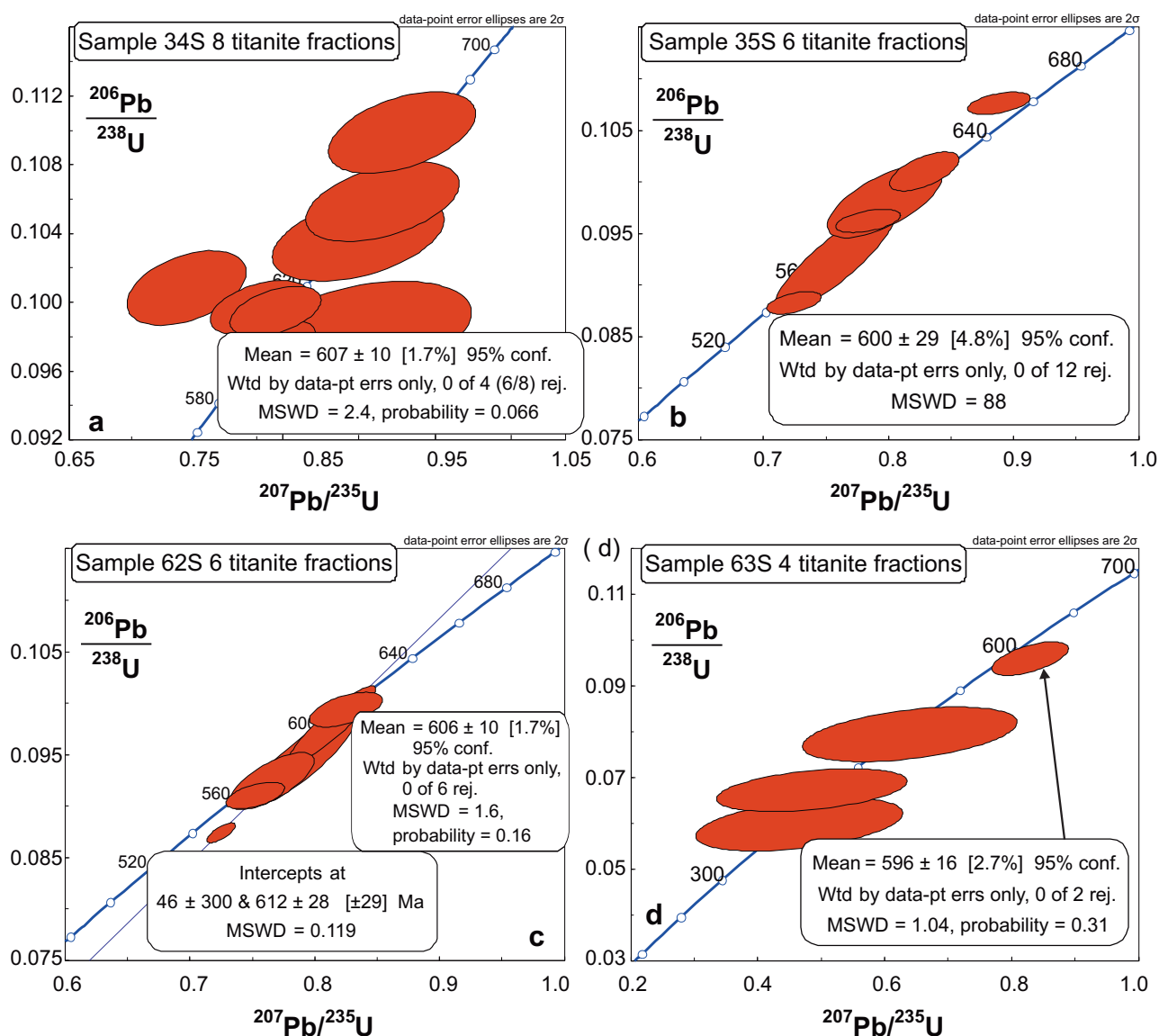


Figure 12. Titanite concordia diagrams: (a) eight fractions from sample 34S, the oldest being 671 ± 11 Ma. The four youngest ones give a $^{206}\text{Pb}/^{238}\text{U}$ mean age of 607 ± 10 Ma; (b) concordia of six fractions from sample 35S, the oldest having an age of 657.5 ± 5.2 Ma and all give a mean age of 600 ± 29 Ma; (c) six concordant fractions from sample 62S with one slightly discordant fraction. The oldest fraction has an age of 610.6 ± 7.6 Ma. The three oldest fractions have a mean age of 606 ± 10 Ma, identical within error with the upper intercept age of 612 ± 28 Ma when all the fractions are considered; (d) concordia of four dissimilar fractions from sample 63S with the oldest giving an age of 596 ± 16 Ma. The youngest concordant titanite age (374 ± 28 Ma) is recorded by fraction four (Table 2) and probably indicates a reset age.

tectono-magmatic peak of the Pan-African orogeny in Sudan. Fourthly, the 607 ± 10 Ma upper intercept age and fifthly, the 554.2 ± 2.1 Ma concordant age of the colourless zircon population (Figures 10c & 11a), are thought to represent the peak (e.g., Kröner & Stern 2004; Shang *et al.* 2010a) and the waning phase, respectively, of the Pan-African orogeny in Sudan.

The discordant nature of most U-Pb data in this study suggests, in the absence of overgrown metamorphic zircon rims (Figure 7), that the zircons have suffered Pb-loss. As a consequence, fractions that show greater degrees of discordance are thought to have suffered more Pb-loss than the less discordant ones. It appears that the degree of

Table 4. Sm, Nd, Rb and Sr abundances and isotopic composition.

Sample	Sm ppm	Nd ppm	$^{147}\text{Sm}/$ ^{144}Nd	$^{143}\text{Nd}/$ $^{144}\text{Nd} \pm 2\sigma_m$	$^{143}\text{Nd}/^{144}\text{Nd}$ 640 Ma	ϵNd 640 Ma	ϵNd 0 Ma	$T_{\text{DM}}/$ Ma	Rb ppm	Sr ppm	$^{87}\text{Rb}/^{86}\text{Sr}$	$^{87}\text{Sr}/^{86}\text{Sr} \pm 2\sigma_m$	Sr initial 640 Ma
34S	1.15	5.8	0.11993	0.512752 (08)	0.512249	8.52	2.22	671	7	154	0.1330	0.703709 (09)	0.702495
35S	5.96	37	0.09743	0.512649 (07)	0.512240	8.35	0.21	676	92	255	1.0471	0.711948 (06)	0.702389
61S	4.53	26.2	0.10457	0.512570 (10)	0.512131	6.22	-1.33	832	73	89	2.3784	0.725724 (08)	0.704011
62S	4.4	25.4	0.10477	0.512511 (12)	0.512072	5.05	-2.48	917	69	381	0.5228	0.707597 (08)	0.702824
63S	9.939	80.15	0.07500	0.512571 (09)	0.512256	8.66	-1.31	653	73	83	2.5499	0.726582 (08)	0.703303

σ_m error of measured value; Nd model ages after Goldstein *et al.* (1984).

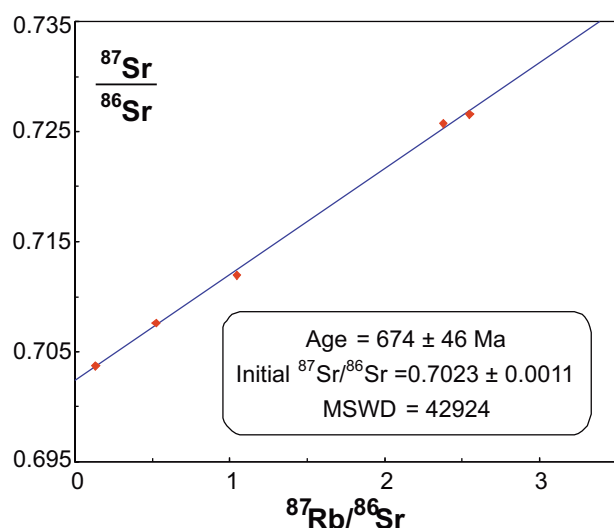


Figure 13. Rb-Sr errorchron of five whole-rock samples with an age of 674 ± 46 Ma, being almost the average of Neoproterozoic zircon ages, despite the very high MSWD; notice that the initial Sr value is identical with those calculated using the 640 Ma zircon age.

discordance decreases with decreasing age, with the Archaean smoky zircons showing greater degrees of discordance than the Neoproterozoic yellow, reddish yellow and colourless zircon populations (Figures 10 & 11).

Lower intercept ages often mark the timing of the Pb-loss inducing event. In this study, all discordant Neoproterozoic zircons (Figure 10) show variable and very young close to zero lower intercept ages, suggesting that Pb-loss in these zircons has continued up till the present and was not episodic. Such continuous Pb-loss due to diffusion and leaching has been known for a long time (e.g., Corfu & Ayres 1984; Corfu 2000). However, the Archaean zircon population yields a Neoproterozoic lower intercept

age (602 ± 350 Ma; Figure 11b) indistinguishable within error from all Neoproterozoic zircon and titanite ages in this study. Thus, it can be concluded that the Neoproterozoic events had affected the studied basement rocks in central North Sudan, leading to Neoproterozoic zircon and titanite crystallization. We interpret these events to correspond to the Pan-African tectono-metamorphic and magmatic episodes in East Africa, due to the collision of East and West Gondwana (Shang *et al.* 2010a) which resulted in the formation of Greater Gondwana or Pannotia (Stern 2008). The 554.2 ± 2.1 Ma concordant zircon age (Figure 11a) further indicates that such a distinct regional event as the Pan-African orogeny had not occurred again since 554.2 Ma. This however, does not exclude the occurrence of more localized events along shear corridors and fault zones and regional events whose tectono-thermal degree had not attained zircon U-Pb system reset temperatures.

Titanite U-Pb Age Implications

Fractions with the highest mean concordant titanite U-Pb ages (e.g., 671 ± 11 for sample 34S; 618.4 ± 8.3 Ma for sample 35S; 610.6 ± 7.6 Ma for sample 62S, and 596 ± 16 Ma for sample 63S) are unsurprisingly younger than the zircon ages from the same rock samples (Figures 10 & 11). This is consistent with the closure temperatures for the two minerals in magmatic-metamorphic systems (550 to 700°C for titanite, e.g., Scott & Onge 1995; Miller 2001; 850 to 1000°C for zircon, e.g., Cherniak & Watson 2001; Cherniak *et al.* 2004), indicating that the zircon U-Pb clock had started while titanite was still crystallizing. Titanite mean ages of ca. 600 Ma (Figure 12), in conformity with the youngest zircon ages, are

interpreted to mark the peak age of the Pan-African tectono-metamorphic event in Sudan. Titanite mean ages as young as 374 ± 28 Ma are thought to have been reset, apparently, by a localized post-emplacment tectono-metamorphic overprint (Shang *et al.* 2010a) whose thermal regime was sufficient to reset the titanite U-Pb system but not the zircon U-Pb system that requires much hotter conditions.

Petrogenetic Considerations

Geochemistry – The major element chemistry of the studied rocks with high Na_2O contents (Table 1) is similar to the composition of highly sodic granitoids (e.g., TTGs; Figure 6a, b). High modal quartzofeldspathic mineral contents with only biotite and amphibole as mafic phases tend to confirm the TTG affinity of the studied rocks. However, only two samples (36S, 62S) show similar REE patterns to those of Archaean TTGs (Figure 8a) and three others show post-Archaean granitoid features, namely a markedly negative Eu anomaly and higher HREE content (Figure 8b). In the normalized $\text{Yb}-(\text{La}/\text{Yb})_N$ diagram (Figure 14), all the analyzed samples plot in the field of post-Archaean granitoids, but three plot in the overlapping field between Archaean TTG and post-Archaean granitoids, suggesting a mixture of melts from rocks with chemical features characteristic

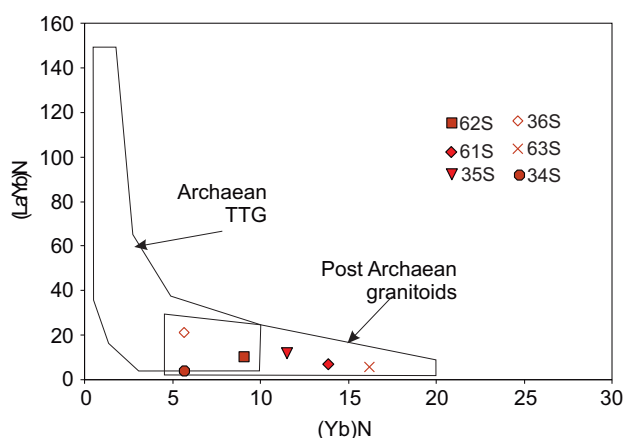


Figure 14. $\text{Yb}_N-(\text{La}/\text{Yb})_N$ diagram showing Archaean and post-Archaean granitoid REE fields and their overlap zone (e.g., Martin 1993). The Archaean rocks have low Yb contents and strongly fractionated REE patterns while post Archaean granitoids have higher Yb contents and moderately fractionated REE patterns.

of the two geologic eras. In the $\text{Y}+\text{Nb}-\text{Rb}$ and $\text{Y}-\text{Nb}$ diagrams (Figure 15), all the analyzed samples plot in the field of granitoids generated in volcanic arcs above subduction zones. They exhibit strong enrichment in most incompatible elements, with notable negative anomalies in Nb and Ti and strong depletion in heavy REE and Y (e.g., Martin 1993), which are signatures of subduction related magmas. The only exception is

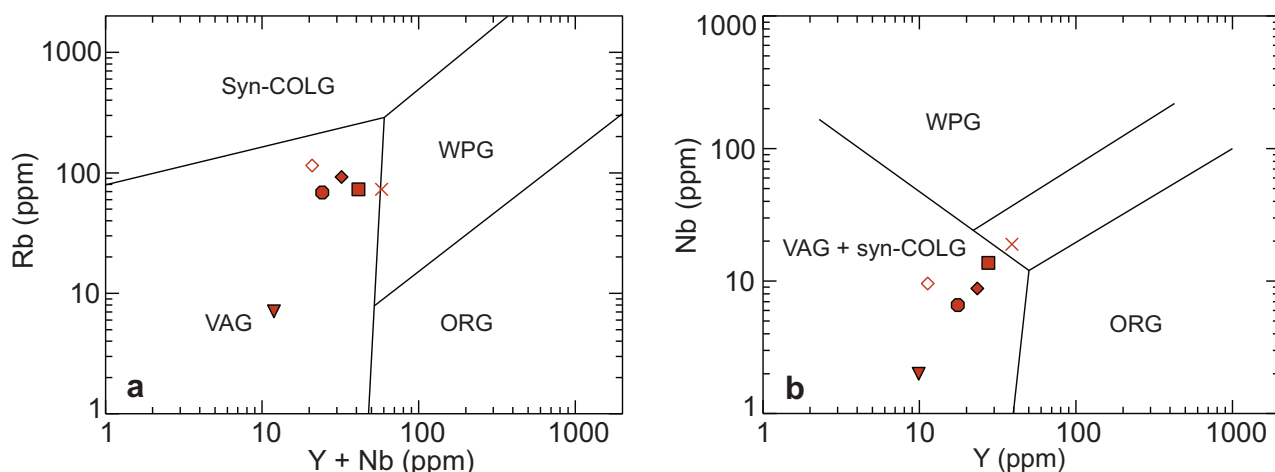


Figure 15. Trace element discrimination plots defining tectonic settings of the samples analyzed in this study: (a) $\text{Y}+\text{Nb}$ versus Rb showing their volcanic arc granitoid (VAG) character and (b) $\text{Y}-\text{Nb}$ showing an additional feature, the syn-collisional granitoid (syn-COLG) signature. These plots mark granitoids that intrude above subduction zones and that are further characterized by negative Nd and Ti anomalies (Figure 7); (WPG– within plate granitoid ; ORG– orogenic granitoid).

sample 34S. Depletion in heavy REE and low Nb/Ta ratios require both garnet and low-Mg amphibole in the restite, whereas moderate to high Sr values allow little if any plagioclase in the restite (e.g., Foley *et al.* 2003). These requirements are met if melting in the source occurs in the hornblende eclogite stability field between 40 and 80 km depth at between 700°C and 800°C. These requirements would be met both in a thick mafic root and a descending slab scenario that would produce identical geochemical features as a result of garnet and hornblende in the source restite.

Isotope Systematics – Sr and Nd isotopes clearly show juvenile sources (Figure 16a). ϵ_{Nd} values are all positive and range from +5.05 to +8.66. These data indicate derivation from a source with a time-integrated depletion in Nd relative to Sm, consistent with an interpretation that, prior to the Neoproterozoic, Nd evolved in a strongly depleted chemical reservoir such as the upper mantle (Liégeois & Stern 2009; Shang *et al.* 2010b). Significant involvement of old crust in magma genesis should result in a strongly negative ϵ_{Nd} and this is not observed for any of the samples.

To determine the mean age of the protolith of a geological unit, Nd TDM model ages are a very powerful tool as they consider the whole-rock and thus magma sources (DePaolo 1983). The principle of the method is to calculate at what age the sample had the $^{143}\text{Nd}/^{144}\text{Nd}$ of the depleted mantle, thus approximating the age of the extraction of the melt (and fractionation of Sm/Nd) from its source. Nd TDM model age calculations also assume that the $^{147}\text{Sm}/^{144}\text{Nd}$ of the rock remained constant since its generation, since REE are difficult to mobilize except in melts, and that it was derived from a depleted mantle that is isotopically approximated by the model. We have used the depleted mantle models of Goldstein *et al.* (1984). However, complications occur if enriched lithospheric mantle was the magma source, or if the igneous rocks were generated from partial melting of much older crust. In such cases a two-stage calculation can be performed, but this is not needed in this study, nor would such a calculation lead to significantly different Nd model ages.

Nd evolution through time for the analyzed samples is shown in Figure 16b. The TDM model age

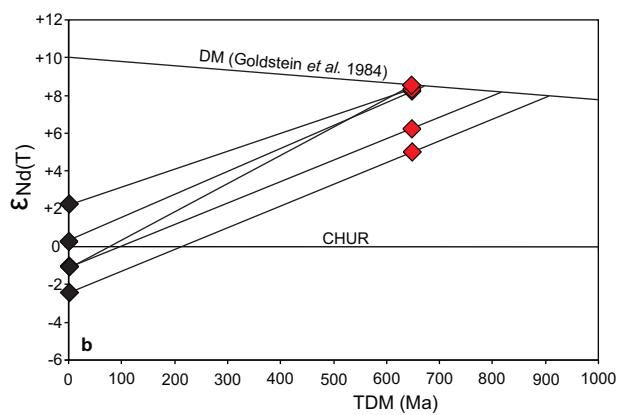
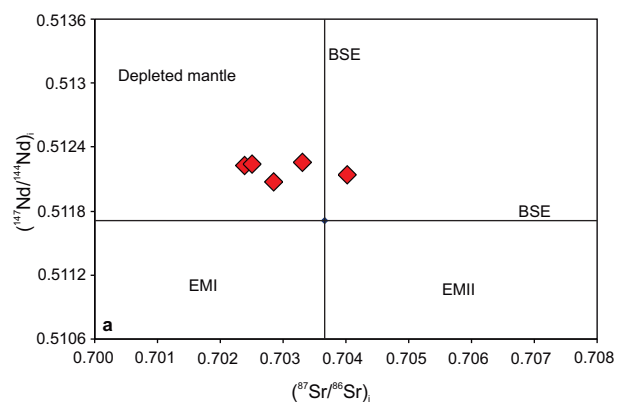


Figure 16. Isotope diagrams: (a) Initial $^{87}\text{Sr}/^{86}\text{Sr}_i$ versus initial $^{143}\text{Nd}/^{144}\text{Nd}(t)$ showing depleted mantle isotope signature of the studied samples; (b) Nd isotopic evolution through time for the studied samples displaying the TDM model ages (intersection with the Goldstein *et al.* (1984) evolution curve for the depleted mantle). The various symbols present on the evolution lines are placed at 640 Ma zircon age. CHUR– chondritic uniform reservoir; DM– depleted mantle; BSE– bulk silicate Earth; EMI– enriched mantle I; EMII– enriched mantle II.

is given by the intersection of the sample line with the DM curve. The juvenile nature of the studied samples is confirmed by the Nd model ages which are closely similar to or slightly older than the zircon ages. This demonstrates that the studied granitoid basement is dominated by juvenile additions from the mantle during Neoproterozoic time. There may be a minor contribution of much older continental crust and/or sediments that cannot be identified isotopically, but significant contributions of older materials should result in a larger spread of Nd model ages, reflecting a mixture between juvenile crustal additions and older crust (e.g., Liégeois & Stern 2009), although

the spread seems to be minimal. A similar variability and shift towards more radiogenic values should also be observed for initial $^{87}\text{Sr}/^{86}\text{Sr}$ values, which instead also cluster tightly around values expected for Neoproterozoic asthenospheric mantle (Table 4, Figure 16a). Both Nd and Sr isotopes as shown in Figure 16a thus portray the depleted signature of the analyzed granitoids which may characterize a juvenile Neoproterozoic crust or the mantle. Consequently, such a protolith must constitute large parts of the lower crust or mantle in the Halfa terrane (e.g., Shang *et al.* 2010b).

The Archaean Zircon Age Paradox

Zircon ages are normally interpreted to represent ages of rocks or tracts of terranes from which they are separated. But it has also been shown that, though robust, zircon ages relate to the ages of the mineral but not necessarily the rock (Hargrove *et al.* 2006; Kennedy *et al.* 2004, 2005; Ali *et al.* 2009). Combining both U-Pb zircon and Sm-Nd whole-rock methods has therefore proven a powerful tool in effectively deciphering genetical relationships between zircon and rock in complex geologic terranes, and determining whether or not the crust is juvenile, and the extent to which it has interacted with ancient crust or sediments (e.g., Küster *et al.* 2008; Liégeois & Stern 2009 and references therein).

In this study, the Palaeoproterozoic $^{206}\text{Pb}/^{238}\text{U}$ and $^{207}\text{Pb}/^{235}\text{U}$ apparent ages (1734 to 2095 Ma) in addition to Archaean $^{207}\text{Pb}/^{206}\text{Pb}$ apparent ages (2606 to 2821 Ma; Table 2) and particularly the mid-Archaean upper discordia intercept age (3025 ± 380 Ma) of the smoky zircon fractions from sample 34S (Figure 11b), first brought in the concept that there may be an Archaean crustal fragment in central North Sudan. But the much younger whole-rock Nd model ages than these zircon pre-Neoproterozoic ages, changed the whole story. In fact, Neoproterozoic Nd model ages of 653 to 917 Ma (Table 4) are very similar to or slightly older than the Neoproterozoic zircon ages obtained (554 to 728 Ma; Figures 10 & 11). This indicates the juvenile nature of this Neoproterozoic magmatism that is confirmed by the positive ϵ_{Nd} values and the low Sr initial ratios (Table 4). This clearly shows that the smoky Archaean zircons are inherited and therefore have no bearing to the age of the granitoids investigated. This pre-Neoproterozoic

zircon age paradox seems not to be peculiar to the studied granitoids in central North Sudan. In the Arabian Nubian Shield for instance, pre-Neoproterozoic zircons are increasingly recognized in juvenile Neoproterozoic igneous rocks (Kennedy *et al.* 2004, 2005; Hargrove *et al.* 2006; Ali *et al.* 2009). Xenocrystic zircons are proportionately most abundant in mafic lavas. This is especially so in the Eastern Desert of Egypt, where relatively abundant Palaeoproterozoic and Archaean xenocrystic zircons have been found in metamorphosed Neoproterozoic basalts, gabbros, andesites and dolerite (Ali *et al.* 2009).

The Sr and Nd isotopic compositions relate to the studied magma and its source (Liégeois & Stern 2009). Sr and Nd analyses of various rock types in an area can thus be considered as representative of the studied crust. This is not so for inherited zircons. Zircon is a very resilient mineral, difficult to dissolve or to destroy and, except in an alkaline-peralkaline environment, it keeps the memory of the different stages of crystallization that it experienced (e.g., Bendaoud *et al.* 2008). It has been demonstrated that zircon can survive in the mantle up to 1500°C and 20 GPa, equivalent to 600 km depth in the Earth (e.g., Tange & Takahashi 2004). Some detrital zircons carried by deep subduction into the diamond zone survive (e.g., Claoué-Long *et al.* 1991; Hermann *et al.* 2001). Zircons formed in the crust may also be carried into the mantle by delamination of dense lower crust (Kay & Kay 1993). Regardless of how zircons formed in the crust are introduced into the mantle, they are resilient enough to even survive extensive melting and be carried back to the surface in magmas. This has been the explanation used for inherited ancient zircons in mid-Atlantic ridge MORB-type gabbros (e.g., Pilot *et al.* 1998; Belyatsky *et al.* 2008). Inherited zircons found in some ophiolites (e.g., Pallister *et al.* 1988; Hargrove *et al.* 2006; Whattam *et al.* 2006) probably originated in this manner. Old zircons can also be incorporated in magmas when clastic sediments are assimilated (e.g., Ali *et al.* 2009; Hargrove *et al.* 2006). Regardless of the precise way in which old zircons become xenocrysts in younger igneous rocks, it is clear that this can occur in mantle-derived melts and thus be incorporated in juvenile crust, without the need that significant tracts of ancient crust existed at the site of juvenile crust formation. This explains the Archaean

zircon age paradox in central North Sudan and demonstrates that combining U-Pb zircon ages and Nd TDM model ages is a powerful tool (e.g., Zhang *et al.* 2005; Küster *et al.* 2008).

Implications for Geodynamics of the Saharan Metacraton Crust

Geochronological data in this study show the presence of an Archaean xenocrystic zircon in juvenile Neoproterozoic crust that survived Neoproterozoic mantle events. Furthermore, Neoproterozoic age data are similar to combined ring complex and basement granite and migmatite data described in other localities in central North Sudan (Shang *et al.* 2010a, b), with far-reaching geodynamic implications. The inherited Archaean zircon shows its resilience and the juvenile nature of the magmatism indicates the involvement of the asthenosphere. This magmatism could have thus been induced either by delamination of the asthenospheric mantle as a response to thickening during a previous collisional orogenic stage (Turner 1996; Mushkin *et al.* 2003) or break-off of a subducted slab (Davies & von Blanckenburg 1995; Whalen *et al.* 2006) causing melting and upwelling of

the hot asthenosphere. Given the geological setting in northeast Africa, we favour the former scenario. In fact, this scenario, characterized in the region by the collisional contact between East and West Gondwana in the Egyptian Eastern Desert, has been suggested to explain the origin of Neoproterozoic alkaline magmatism of similar age (707–718 Ma e.g., Shang *et al.* 2010b) to the Sudan granitoids studied here (702 to 728 Ma; Figure 10d–f). It is therefore highly probable that the emplacement of the granitoid basement north of Delgo was induced by the same collisional event as in the north, in the Egyptian Eastern Desert (e.g., Ali *et al.* 2009; Liégeois & Stern 2009 and references therein) (Figure 17b). The latest Neoproterozoic zircon crystallization ages (554 to 630 Ma; Figures 10a–c & 11a) show that the studied basement granites were overprinted by the local 640–580 Ma Keraf transposition, one of the features of the Pan-African event at the eastern Saharan Metacraton boundary, that induced HT metamorphism and the intrusion of post-collisional granitoids (Abdelsalam *et al.* 1998; Küster *et al.* 2008). These activities correspond to the formation of Greater Gondwana or Pannotia (Stern 2008; Figure 17c).

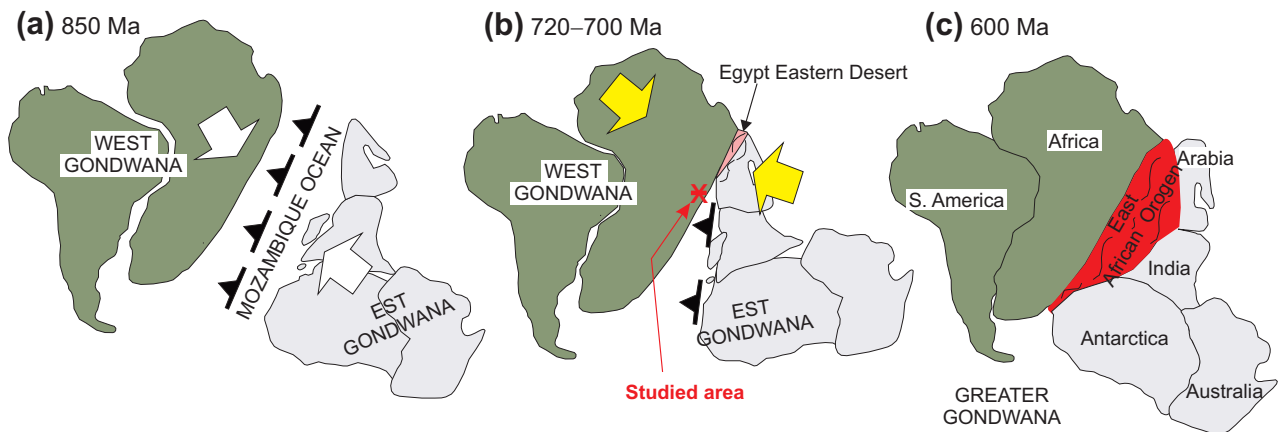


Figure 17. Gondwana during the Neoproterozoic, modified after Abdelsalam & Stern (1996): (a) Mozambique Ocean lies between East and West Gondwana at ~850 Ma as they drift towards each other with ensuing tectono-metamorphic activities. (b) Between ca. 850 and 620 Ma, the Saharan Metacraton in Sudan was ‘quiet’ without orogenic activity. However, by ca. 720 and 700 Ma the Saharan Metacraton experienced intraplate anorogenic magmatism (Shang *et al.* 2010b), attributed to the induced effect of the first collisional contact between East and West Gondwana in the north that is characterized by the 750–720 Egyptian desert gneiss terrane and that lead to the thickening of the asthenospheric mantle in the south and the event of sodic-alkaline magmatism. (c) By ca. 600 Ma: completion of East and West Gondwana collision in the south (Sudan). This process continued further south by the formation of the Mozambique belt marking this suture zone and the final amalgamation of East and West Gondwana to form Greater Gondwana by 560 Ma. The 5000 km long stretch of the East African Orogen comprising the Arabian-Nubian Shield in the north and the Mozambique belt to the south marks the East and West Gondwana collision belt.

Conclusions

The Sudan basement is composed of a variety of rock types including Neoproterozoic granitoids of crustal and juvenile sources. Primitive granitoids so far reported in the Sudan basement are mostly potassic alkaline, but the present study reveals another set of juvenile granites that are sodic alkaline. Major and REE geochemistry show that these Neoproterozoic juvenile sodic granitoids paradoxically combine typical Archaean TTG-like character with post-Archaean granitoid-like features. Zircon and titanite U-Pb data indicate a strong latest Neoproterozoic tectono-metamorphic and tectono-magmatic overprint. But zircon populations, including both Neoproterozoic and Archaean populations, suggest a complicated history. This is, however, unravelled by combining zircon U-Pb and whole-rock Nd and Sr isotope studies. The later (Nd and Sr isotope) studies, strongly substantiated by Neoproterozoic Nd TDM ages, show juvenile sources with a minimal contribution of continental crustal material. This Neoproterozoic juvenile magmatism defines an Archaean zircon age paradox because the Archaean zircon has not defined an Archaean tract of terrane in the studied Sudan basement. This Archaean zircon age paradox has also been described in the Arabian

Nubian Shield, the Eastern Egyptian Desert as well as at the mid-Atlantic ridge. This study, therefore, shows that combining zircon U-Pb and whole-rock Sr and Nd isotope systematics is very powerful in unequivocally defining the juvenile or crustal character of rocks and tracts of terranes, and, by analogy, further shows the resilience of zircon under mantle conditions.

Acknowledgments

CKS would like to thank the co-authors of this paper for their scientific support. Special thanks go particularly to Muharrem Satır for his ever unconditional and fatherly support, and CKS wishes him well in his highly merited and honorable retirement. All members (former and present) of the geochemistry team in Tübingen (including Mozer, Schuman, Batholomä and Stoschek; Reitter and Steinhilber; Fukun, Siebel and Wennemann) should find here on this singular occasion in honour of Muharrem Satır, the retired Chair of Geochemistry, gratitude for everything that has so greatly helped advanced our joint course in the scientific world. Great thanks also go to the Editorial Board of the Turkish Journal of Earth Sciences and to the Reviewers of this paper for their kind considerations.

References

- ABDELSALAM, G.M., LIÉGEOIS, J.P. & STERN, R.J. 2002. Review: the Saharan Metacraton. *Journal of African Earth Sciences* **34**, 119–136.
- ABDELSALAM, G.M. & STERN, R.J. 1996. Mapping Precambrian structures in the Sahara Desert with SIR-C/X-SAR Radar: the Neoproterozoic Kerf Suture, NE Sudan. *Journal of Geophysical Research* **101**, 23063–23076.
- ABDELSALAM, M.G., STERN, R.J., COPELAND, P., EL FAKI, E.M., EL HUR, B. & IBRAHIM, F.M. 1998. The Neoproterozoic Kerf Suture in NE Sudan: sinistral transpression along the eastern margin of West Gondwana. *Journal of Geology* **106**, 133–147.
- ALÍ, K.A., STERN, R.J., MANTON, W.I., KIMURA, J.I. & KHAMEES, H.A. 2009. Geochemistry, Nd isotopes and U-Pb SHRIMP zircon dating of Neoproterozoic volcanic rocks from the Central Eastern Desert of Egypt: new insights into the ~750 Ma crust forming event. *Precambrian Research* **171**, 1–22.
- ANDRÉ, L., KLERKX, J. & BUSREWIL, M.T. 1991. Geochemical and Rb–Sr isotopic data on felsic rocks from the Jabal al Aawaynat alkaline intrusive complex (SE Libya). In: SALEM, M.J., BUSREWIL, M.T. & BEN ASHOUR, A.M. (eds), *The Geology of Libya*. Elsevier, Amsterdam 7, 2511–2527.
- BELYATSKY, B., LEPEKHINA, E., ANTONOV, A., SHULIATIN, O. & SERGEEV, S. 2008. Age and genesis of accessory zircon from MAR gabbroids. *Geophysical Research Abstracts* **10**, EGU2008-A-01314.
- BENDAOU, A., OUZEGANE, K., GODARD, G., LIÉGEOIS, J.P., KIENAST, J.R., BRUGUIER, O. & DRARENI, A. 2008. Geochronology and metamorphic P-T-X evolution of the Eburnean granulite-facies metapelites of Tidjenouine (Central Hoggar, Algeria): witness of the LATEA metacratonic evolution. In: ENNIH, N. & LIÉGEOIS, J.-P. (eds), *The Boundaries of the West African Craton*. Geological Society, London, Special Publications **297**, 111–146.
- BLACK, R. & LIÉGEOIS, J.P. 1993. Cratons, mobile belts, alkaline rocks and continental lithospheric mantle: the Pan-African testimony. *Journal of the Geological Society, London* **150**, 89–98.
- BOYNTON, W.V. 1984. Geochemistry of the rare earth elements: meteorite studies. In: HENDERSON, P. (ed), *Rare Earth Element Geochemistry*. Elsevier, 63–114.
- CAHEN L., SNELLING N.J., DELHAL J., VAIL J.R., BONHOMME M. & LEDENT, D. 1984. *The Geochronology and Evolution of Africa, Phanerozoic Anorogenic Igneous Activity in Africa*. Clarendon Press, 385–392.

- CHERNIAK, D.J. & WATSON, E.B. 2001. Pb diffusion in zircon. *Chemical Geology* **172**, 5–24.
- CHERNIAK, D.J., WATSON, E.B., GROVE, M. & HARRISON, T.M. 2004. Pb diffusion in monazite: a combined RBS/SIMS study. *Geochimica et Cosmochimica Acta* **68**, 829–840.
- CLAOUÉ-LONG, J.C., SOBOLEV, N.V., SHATSKY, V.S. & SOBOLEV, A.V. 1991. Zircon response to diamond-pressure metamorphism in the Kokchetav massif, USSR. *Geology* **19**, 710–713.
- CONTICELLI, S., MANETTI, P., CAPALDI, G. & POLI, G. 1995. Petrology, mineralogy and isotopes in olivine mela-nephelinites, basanites and carbonatites from Uwaynat region, south east Libya: inferences on their genesis. *Africa Geoscience Review* **2**, 227–245.
- CORFU, F. 2000. Extraction of Pb with artificially too-old ages during stepwise dissolution experiments on Archaean zircon. *Lithos* **53**, 279–291.
- CORFU, F. & AYRES, L.D. 1984. U-Pb ages and genetic significance of heterogeneous zircon populations in rocks from the Favourable Lake area, northwestern Ontario. *Contributions to Mineralogy and Petrology* **88**, 86–101.
- DAVIES, J.H. & VON BLANCKENBURG, F. 1995. Slab break-off, a model of lithosphere detachment and its test in the magmatism and deformation of collisional orogens. *Earth Planetary Science Letters* **129**, 85–102.
- DENKLER, T., FRANZ, G. & SCHANDELMEIER, H. 1994. Tectonometamorphic evolution of the Neoproterozoic Delgo suture zone, Northern Sudan. *Geologische Rundschau* **83**, 578–590.
- DEPAOLO, D.J. 1983. The mean life of continents: estimates of continent recycling rates from Nd and Hf isotopic data and implications for mantle structure. *Geophysical Research Letters* **10**, 705–708.
- DOSTAL, J., DUPUY, C. & POIDEVIN, J.L. 1985. Geochemistry of Precambrian basaltic rocks from the Central African Republic (equatorial Africa). *Canadian Journal of Earth Sciences* **22**, 653–662.
- EL SHAZLY, E.M., HASHAD, A.H., SAYYAH, T.A. & BASSYUNI, F.A. 1973. Geochronology of Abu Swayal area, South-eastern Desert. *Egyptian Journal of Geology* **17**, 1–18.
- FLECK, R.J., COLEMAN, R.G., CORNWALL, H.R., GREENWOOD, W.R., HADLEY, D.G., PRINZ, W.C., RATTE, J.S. & SCHMIDT, D.L. 1973. *Potassium-argon Geochronology of the Arabian Shield*. United States Department of International Geological Survey, Saudi Arabia Project Report **165**, 1–40.
- FOLEY, S.F., BUHRE, S. & JACOB, D.E. 2003. Evolution of the Archaean crust by delamination and shallow subduction. *Nature* **421**, 249–252.
- GRAVIOU, P. 1984. *Pétrogenèse des magma calco-alcalins: exemple des granitoïdes cadomiens de la région trégoroise (Massif Armoricain)*. Thesis, Université Rennes [unpublished].
- GOLDSTEIN, S.L., O'NIONS, R.K., KEITH, R. & HAMILTON, P.J. 1984. A Sm-Nd isotopic study of atmospheric dusts and particulates from major river systems. *Earth and Planetary Science Letters* **70**, 221–236.
- HARGROVE, U.S., STERN, R.J., GRIFFIN, W.R., JOHNSON, P.R. & ABDELSALAM, M.G. 2006. From island arc to craton: time scales of crustal formation along the Neoproterozoic Bi'r Umq suture zone. *Saudi Geological Survey, Kingdom of Saudi Arabia*, p. 69.
- HASHAD, A.H., SAYYAH, T.A., EL KHOLY, S.B. & YOUSSEF, A. 1972. Rb/Sr isotopic age determination of some basement Egyptian granites. *Egyptian Journal of Geology* **16**, 269–281.
- HARMS, U., DARBYSHIRE, D.P.F., DENKLER, T., HENGST, M. & SCHANDELMEIER, H. 1994. Evolution of the Neoproterozoic Delgo suture zone and crustal growth in northern Sudan: geochemical and radiogenic isotope constraints. *Geologische Rundschau* **83**, 591–603.
- HARMS, U., SCHANDELMEIER, H. & DARBYSHIRE, D.P.F. 1990. Pan-African reworked early/middle Proterozoic crust in NE Africa west of the Nile: Sr and Nd isotope evidence. *Journal of the Geological Society, London* **147**, 859–872.
- HARRIS N.B.W., HAWKESWORTH, C.J. & RIES, A.C. 1984. Crustal evolution in north-east and east Africa from model Nd ages. *Nature* **309**, 773–776.
- HERMANN, J., RUBATTO, D., KORSKOV, A. & SHATSKY, V. 2001. Multiple zircon growth during fast exhumation of diamondiferous, deeply subducted continental crust (Kokchetav Massif, Kazakhstan). *Contributions to Mineralogy and Petrology* **141**, 66–82.
- HUTH, A., FRANZ, G. & SCHANDELMEIER, H. 1984. Magmatic and metamorphic rocks of NW Sudan: a reconnaissance survey. *Berliner geowissenschaftliche Abhandlungen Reihe A* **50**, 7–21.
- JACOBSEN, S.B. & WASSERBURG, G.J. 1980. Sm-Nd isotopic evolution of chondrites. *Earth and Planetary Science Letters* **50**, 139–155.
- KAY, R.W. & KAY, S.M. 1993. Delamination and delamination magmatism. *Tectonophysics* **219**, 177–189.
- KENNEDY, W.Q. 1965. The influence of basement structure on the evolution of the coastal (Mesozoic and Tertiary) basins of Africa. *Salt Basins around Africa*. Institute of Petroleum, London, 7–16.
- KENNEDY, A., JOHNSON, P.R. & KATTAN, F.H. 2004. *SHRIMP Geochronology in the Northern Arabian Shield. Part I: Data Acquisition*. Saudi Geological Survey Open File Report, v. SGS-OF-2004-11.
- KENNEDY, A., JOHNSON, P.R. & KATTAN, F.H. 2005. *SHRIMP Geochronology in the Northern Arabian Shield. Part II: Data Acquisition 2004*. Saudi Geological Survey Open File Report, v. SGS-OF-2005-10.
- KLERKX, J. & DEUTSCH, S. 1977. Résultats préliminaires obtenus par la méthode Rb/Sr sur l'âge des formations précambriennes de la région d'Uweinat (Libye). *Musée Royal Afrique Centrale, Département Géologie Minéralogie Rapport Annuel* **1976**, 83–94.

- KRÖNER, A. & STERN, R.J. 2004. Pan-African orogeny. *Encyclopedia of Geology* **1**, 1–12.
- KRÖNER, A., STERN, R.J., DAWOUD, A.S., COMPSTON, W. & REISCHMANN, T. 1987. The Pan-African continental margin in northeastern Africa: evidence from a geochronological study of granulites at Sabaloka, Sudan. *Earth and Planetary Science Letters* **85**, 91–104.
- KÜSTER, D. & HARMS, U. 1998. Post-collisional potassic granitoids from the southern and northwestern parts of the Late Neoproterozoic East African Orogen: a review. *Lithos* **45**, 177–195.
- KÜSTER, D. & LIÉGEOIS, J.P. 2001. Sr, Nd isotopes and geochemistry of the Bayuda Dessert high-grade metamorphic basement (Sudan): an early Pan-African oceanic convergent margin, not the edge of the East Saharan ghost craton. *Precambrian Research* **109**, 1–23.
- KÜSTER, D., LIÉGEOIS, J.-P., MATUKOV, D., SERGEEV, S. & LUCASSEN, F. 2008. Zircon geochronology and Sr, Nd, Pb isotope geochemistry of granitoids from Bayuda Desert and Sabaloka (Sudan): evidence for a Bayudian event (920–900 Ma) preceding the Pan-African orogenic cycle (860–590 Ma) at the eastern boundary of the Saharan Metacraton. *Precambrian Research* **164**, 16–39.
- LIÉGEOIS, J.P., BLACK, R., NAVEZ, J. & LATOUCHE, L. 1994. Early and late Pan-African orogenies in the Air assembly of terranes (Tuareg Shield, Niger). *Precambrian Research* **67**, 59–88.
- LIÉGEOIS, J.P. & STERN, R.J. 2009. Sr-Nd isotopes and geochemistry of granite-gneiss complexes from the Meatiq and Hafafit domes, Eastern Desert, Egypt: no evidence for pre-Neoproterozoic crust. *Journal of African Earth Sciences* **57**, 31–40.
- LUDWIG, K. 2003. *Isoplot/Ex, Version 3.00: A Geochronological Toolkit for Microsoft Excel*. Berkeley Geochronology Center Special Publications No. 4.
- LUGMAIR, G.W. & MARTI, K. 1978. Lunar initial $^{143}\text{Nd}/^{144}\text{Nd}$: differential evolution of the lunar crust and mantle. *Earth and Planetary Science Letters* **39**, 349–357.
- MARTIN, H. 1987. Petrogenesis of Archaean trondhjemites, tonalites and granodiorites from Eastern Finland: major and trace element geochemistry. *Journal of Petrology* **28**, 921–953.
- MARTIN, H. 1993. The mechanisms of petrogenesis of the Archaean continental crust-comparison with modern processes. *Lithos* **30**, 373–388.
- MILLER, B.V. 2001. *U-Pb Closure Temperatures and Metamorphic Closing Rates from Coexisting Rutile and Titanite*. 50th Annual Meeting, Advances in Geochronology and Thermochronology in the Appalachian Orogen.
- MUSHKIN, A., NAVON, O., HALICZ, L., HARTMANN, G. & STEIN, M. 2003. The petrogenesis of A-type magmas from the Amram Massif, southern Israel. *Journal of Petrology* **44**, 815–832.
- PALLISTER, J.S., STACEY, J.S., FISCHER, L.B. & PREMIO, W.R. 1988. Precambrian ophiolites of Arabia: geologic settings, U-Pb geochronology, Pb-isotope characteristics, and implications for continental accretion. *Precambrian Research* **38**, 1–54.
- PARRISH, R.R. 1987. An improved micro-capsule for zircon dissolution in U-Pb geochronology. *Chemical Geology* **66**, 99–102.
- PILOT, J., WERNER, C.D., HAUBRICH, F. & BAUMANN, N. 1998. Palaeozoic and Proterozoic zircons from the Mid-Atlantic ridge. *Nature* **393**, 676–679.
- POTTS, P.J. & WEB, P.C. 1992. X-ray fluorescence spectrometry. *Journal of Geochemical Exploration* **4**, 251–296.
- SCHANDELMEIER, H., RICHER, A., HARMS, U. & ABDEL-RAHMAN, E.M. 1990. Lithology and structure of the late Proterozoic Jebel Rahib fold-and-thrust belt (SW Sudan). *Berliner Geowissen Abher (A)* **120.1**, 15–30.
- SCHANDELMEIER, H., WIPFLER, E., KÜSTER, D., SULTAN, M., BECKER, R., STERN, R.J. & ABDELSALAM, M.G. 1994. Atmur-Delgo suture: a Neoproterozoic oceanic basin extending into the interior of northeast Africa. *Geology* **22**, 563–566.
- SCOTT, D.J. & ST-ONGE, M.R. 1995. Constraints on Pb closure temperature in titanite based on rocks from the Ungava orogen, Canada: implications for U-Pb geochronology and P-T-t path determinations. *Geology* **23**, 1123–1126.
- SHANG, C.K., SATIR, M., MORTEANI, G. & TAUBALD, H. 2010a. Zircon and titanite age evidence for coeval granitization and migmatization of the early Middle and early Late Proterozoic Saharan Metacraton; example from the central North Sudan basement. *Journal of African Earth Sciences* **57**, 492–524.
- SHANG, C.K., MORTEANI, G., SATIR, M. & TAUBALD, H. 2010b. Neoproterozoic continental growth prior to Gondwana assembly: constraints from zircon-titanite geochronology, geochemistry and petrography of ring complex granitoids, Sudan. *Lithos* **118**, 61–81.
- STACEY, J.S. & KRAMERS, J.D. 1975. Approximation of terrestrial lead isotope evolution by a two-stage model. *Earth and Planetary Science Letters* **26**, 207–221.
- STEIGER, R.H. & JÄGER, E. 1977. Subcommission on geochronology: conventions of the use of decay constants in geochronology and cosmochronology. *Earth and Planetary Science Letters* **36**, 359–362.
- STERN, R.J. 1994. Neoproterozoic (900–550 Ma) arc assembly and continental collision in the East African Orogen: implications for the consolidation of Gondwanaland. *Annual Review of Earth and Planetary Sciences* **22**, 319–351.
- STERN, R.J. 2008. Neoproterozoic crustal growth: the solid earth system during a critical episode of earth history. *Gondwana Research* **14**, 33–50.
- STERN, R.J., KRÖNER, A., REISCHMANN, T., BENDER, R. & DAWOUD, A.S. 1994. Precambrian basement around Wadi Halfa: a new perspective on the evolution of the Central Saharan Ghost craton. *Geologische Rundschau* **93**, 564–577.
- TANGE, Y. & TAKAHASHI, E. 2004. Stability of the high-pressure polymorph of zircon (ZrSiO_4) in the deep mantle. *Physics of the Earth and Planetary Interiors* **143**, 223–229.

- TURNER, S.P. 1996. Petrogenesis of the Late-Delamerian gabbroic complex at Black Hill, South Australia, implications for convective thinning of the lithospheric mantle. *Mineralogy and Petrology* **56**, 51–89.
- WHALEN, J.B., MCNICOLL, V.J., VAN STAAL, C.R., LISSENBERG, C.J., LONGSTAFFE, F.J., JENNER, G.A. & VAN BREEMAN, O. 2006. Spatial, temporal and geochemical characteristics of Silurian collision-zone magmatism, Newfoundland Appalachians, an example of a rapidly evolving magmatic system related to slab break-off. *Lithos* **89**, 377–404.
- WHATTAM, S.A., MALPAS, J., SMITH, I.E.M. & ALI, J.R. 2006. Link between SSZ ophiolite formation, emplacement and arc inception, Northland, New Zealand: U-Pb SHRIMP constraints. *Earth and Planetary Science Letters* **250**, 606–632.
- WHITE, A.J.R. & CHAPPELL, B.W. 1977. Ultrametamorphism and granitoid genesis. *Tectonophysics* **43**, 7–32.
- ZHANG, R.Y., YANG, J.S., WOODEN, J.L., LIOU, J.G. & LI, T.F. 2005. U-Pb SHRIMP geochronology of zircon in garnet peridotite from the Sulu UHP terrane, China: implications for mantle. *Earth and Planetary Science Letters* **237**, 729–743.